

# Daya Bay Absolute Detection Efficiency TechNote

Guofu Cao, Xuefeng Ding, Wenqiang Gu, Gaosong Li, Bryce Littlejohn,  
Jianglai Liu, Yingbiao Liu, David Webber, Jianyi Xu, and Zeyuan Yu  
(Dated: September 4, 2015)

## I. INTRODUCTION

In the Daya Bay data analysis, a wide variety of cuts are applied to data to select with high purity time-coincident trigger pairs that match the characteristics of inverse beta decay products. In order to estimate the total predicted number of detected inverse beta decay events, the total number of target protons and the efficiencies of all signal selection cuts must be estimated.

All cut efficiencies have been estimated in previous Daya Bay publications [1, 2]. Some of these efficiencies remain unchanged in this analysis, and are only briefly described here. A few key efficiencies common to all detectors have been re-calculated utilizing newly-produced comparisons between data and Monte Carlo simulation:

- Gd capture fraction: The fraction of total target IBD interactions whose neutrons capture on Gd.
- Spill-in effects: The fraction of total IBD nGd whose interaction vertex is outside the target.
- Gd capture detection efficiency: The fraction of total nGd IBD above the 6 MeV delayed energy cut.

Previous efficiency and systematics estimates for these key efficiencies were based primarily on observed variations between differing Monte Carlo models and on incomplete data-Monte Carlo comparisons. The improved data-constrained absolute efficiencies will be described below in detail. The re-calculation and application of these key efficiencies and systematics will result in a more reliable measurement of the overall reactor  $\bar{\nu}_e$  flux from Daya Bay. Furthermore, since these key systematics are entirely correlated between all Daya Bay detectors, this re-analysis will have no effect on the best-fit oscillation parameters reported by Daya Bay in the past.

## II. DEFINITION OF EFFICIENCIES

The total number of detected inverse beta decays follows the familiar equation:

$$N_{IBD}(E, t) = \frac{N_p(t)}{4\pi L^2} \epsilon(E) \sigma_{IBD}(E) S(E). \quad (1)$$

The total detection efficiency is defined as the total number of IBD coincidences passing all signal selection cuts over the total number of inverse beta decay interactions in the target region of the detector. The various contributing efficiencies to this overall detection efficiency are defined as follows:

$$\begin{aligned}
\epsilon &= \frac{N_{Tot,Gd,E>6,Other}}{N_{In}} \\
&= \epsilon_{other} \frac{N_{Tot,Gd,E>6}}{N_{In}}, \quad \epsilon_{other} = \frac{N_{Tot,Gd,E>6,other}}{N_{Tot,Gd,E>6}} \\
&= \epsilon_{tail} \epsilon_{other} \frac{N_{Tot,Gd}}{N_{In}}, \quad \epsilon_{tail} = \frac{N_{Tot,Gd,E>6}}{N_{Tot,Gd}} \\
&= \epsilon_{tail} \epsilon_{other} \frac{N_{In,Gd} + N_{Out,Gd}}{N_{In}}, \quad N_{Tot,Gd} = N_{In,Gd} + N_{Out,Gd} \\
&= \epsilon_{tail} \epsilon_{other} \left( \epsilon_{Gd} + \frac{N_{Out,Gd}}{N_{In}} \right), \quad \epsilon_{Gd} = \frac{N_{In,Gd}}{N_{In}} \\
&= \epsilon_{tail} \epsilon_{other} \epsilon_{Gd} \left( 1 + \frac{N_{Out,Gd}}{N_{In,Gd}} \right) \\
&= \epsilon_{tail} \epsilon_{other} \epsilon_{Gd} R_{Spill-in}, \quad R_{Spill-in} = 1 + \frac{N_{Out,Gd}}{N_{In,Gd}}
\end{aligned}$$

Here,  $\epsilon_{Gd}$  is the Gd capture fraction,  $\epsilon_{tail}$  is the nGd detection efficiency,  $R_{Spill-in}$  is the contribution from spill-in events, and  $\epsilon_{other}$  is the combination of all other detection efficiencies.  $N_{In}$  and  $N_{Out}$  are the total events inside the target and outside the target, respectively.  $N_{Gd}$  is the number of events capturing on Gd,  $N_{E>6}$  is the number of events passing the 6 MeV delayed energy cut, and  $N_{other}$  is the number of events passing all other cuts. The efficiency  $\epsilon_{other}$  will not be re-calculated in this TechNote. The remaining factors will be re-calculated in detail below.

### III. CENTER GD CAPTURE FRACTION

The keV-range kinetic energy neutrons created in inverse beta decay interactions in the GdLS thermalize in the detector and capture principally on either H or Gd nuclei. Because of their low capture energy, nH captures are completely excluded from the IBD signal. Thus determining the Gd capture fraction is vital in determining the overall predicted flux normalization. This Gd capture ratio is largely determined by the absolute Gd concentration in the GdLS. The Gd capture ratio resulting from the absolute Gd concentration can be cleanly measured by looking at AD-center events for various non-IBD datasets.

#### A. H/Gd Ratio with Spallation Neutrons

Various H/Gd ratio studies have been conducted utilizing uniformly distributed spallation neutrons. Previous studies [3–5] have utilized the P12A dataset to determine this ratio, a dataset including only AD1 and AD2 data. Spallation neutrons were selected by isolating all detector triggers taking place shortly after an AD muon. Signal regions began 20  $\mu$ s after an AD muon for all studies, extending anywhere from 200 to 300  $\mu$ s. Off-window background subtraction was utilized to subtract backgrounds, utilizing a subtraction window of similar length anywhere from 200 to 500  $\mu$ s after an AD muon. One can define a Gd capture fraction metric by dividing the total number of Gd captures by the total number of captures of all kinds. This can be approximately achieved for AD-center-reconstructed spallation neutrons by selecting similar portions of the capture peaks for nH and nGd captures:

$$\epsilon_{Gd-H} = \frac{N_{Gd}}{N_H + N_{Gd}} = \frac{nCap[5.0, 12.0]}{nCap[1.7, 2.7] + nCap[5.0, 12.0]} \quad (2)$$

This metric is chosen for its simplicity: it does not depend on MC calculations, whose dissimilarity with real data introduces a hard-to-quantify systematic uncertainty. However, this value of this ratio metric will depend partially on the cut energies, since both nH and nGd peaks also contain small tails trailing off at

lower-than-peak energies. The variation in Gd capture fraction with changes in energy cuts will be treated as a source of uncertainty in the measurement.

This analysis focuses mainly on AD-center spallation events by including position cuts in R and Z. Cuts restrict the analysis largely to spallation events constructed in the AD center. Capture times for nH and nGd should be nearly identical, and any difference need not be considered in this analysis. Biases introduced by relative differences in position reconstruction resolutions of nGd and nH are likely to be small, given the uniformly distributed nature of the spallation events well beyond the position cut values.

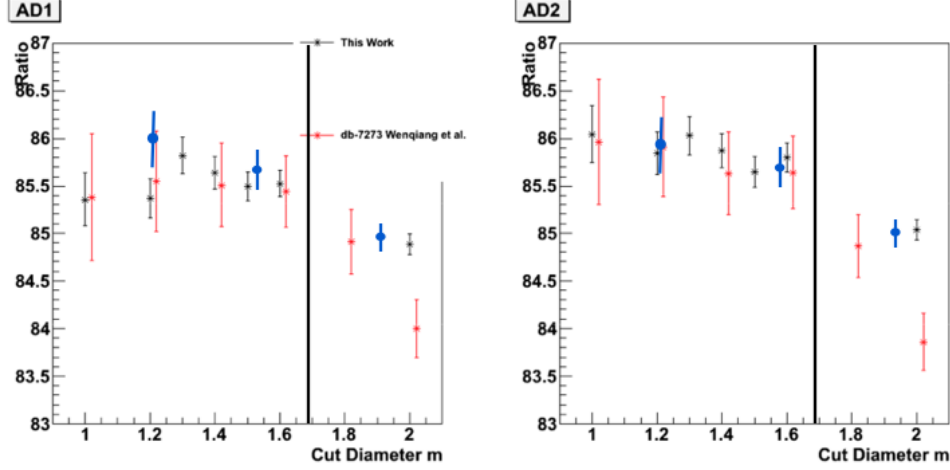


FIG. 1: H/Gd ratio versus position cut diameter. One can see the H/Gd ratio reaches a consistent ratio as the cut approach the AD center, although statistical uncertainty also rises as the cut's stringency is increased.

H/Gd ratios for various position cut diameters are shown in Figure 1. One can see that as the cut value is tightened to the center of the AD, the H/Gd ratio plateaus at a value of roughly 85.6%, as edge effects are removed from the dataset. H/Gd values for the various studies at a cut diameter of 1.2 m are shown in Table I. These studies report very similar values within 0.1%. Furthermore, as the nGd and nH energy cut ranges are varied, H/Gd ratios vary by roughly 0.2%, as shown in Table II. If the length of the background subtraction off-window is varied within a range giving a reasonable nH and nGd tail shape, ratios are consistent to within 0.1%.

Ratios are also in very good agreement between ADs in all cases: if all data from the far-site ADs are combined, the AD-center H/Gd ratio is 85.7% with a 0.4% statistical uncertainty.

Study DocDB #	(6,12)/[(6,12)+(1.8,2.8)] (%)	R,Z Pos Cut (m)
7273	85.5	0.8 m
7524	85.7	0.8 m
7525	85.5	0.8 m

TABLE I: H/Gd ratios for various studies using P12A data. Differences between ADs 1 and 2 are negligible. Uncertainties on these measurement are estimated at roughly 0.5%.

An updated version of this study was done with the full 6-AD dataset [6], producing an H/Gd value of roughly 85.7% within 0.8 m of the AD center, in agreement with previous measurements. **If one adds up total uncertainties from position cuts ( $\pm 0.3\%$  within 1 m of the detector center), energy cuts ( $\pm 0.2\%$ ), background subtraction window ( $\pm 0.1\%$ ), and statistics ( $\pm 0.2\%$ ), the total AD center H/Gd ratio from spallation neutrons is  $85.7\% \pm 0.4\%$ .**

If one includes all events from 1.5-12 MeV in the denominator of the ratio, it changes to 84.1%. This rough measure of combined efficiency will be discussed in a future section, and is in decent agreement with

LE Range (MeV),	HE Range (MeV)	H/Gd Ratio (%)
1.8-2.8	7-9.5	84.5
1-2.8	4-10	84.8
1.5-2.8	4-10	84.9
1.5-2.8	5.5-10	84.8

TABLE II: H/Gd ratios for various energy range selections. In this case, the position cut selection was  $R, |Z| < 0.95$ . One can see the ratio is insensitive to the H and Gd energy definitions, within roughly  $\pm 0.2\%$ .

similar measurements from special ACU sources.

## B. H/Gd Ratio with Special Calibration Runs

Gd capture ratio is an important component for the absolute detection efficiency. In PRL, center Gd capture ratio is combined with spill-out effect as one effective value, assigned with a total 0.8% uncertainty. In this note, we are trying to separate Gd capture ratio out and constrain its uncertainty using various neutron sources deployed during the special ACU calibration in summer 2012.

### 1. Data Analysis

Three different neutron sources, AmC, AmBe and PuC, each with a total neutron rate of  $\sim 1\text{Hz}$ ,  $\sim 6\text{Hz}$ ,  $\sim 1\text{kHz}$  were employed. For data, we use the following analysis cuts to select prompt-delayed pairs:

- flasher cut
- AD muon veto
- $\Delta T < 200\mu s$
- $Multiplicity = 2$
- $1.8\text{MeV} < E_d < 12\text{MeV}$

After the pair selection, there are still accidental backgrounds remaining in the sample, we use the random shuffle method [7] to predict the number and spectrum of accidental background and subtract them from the sample. With a background subtracted sample, Gd capture ratio can be calculated. A combined efficiency  $\epsilon_{Gd-combined}$  can be defined as below:

$$\epsilon_{Gd-combined} = \frac{nCap[6, 12]}{nCap[1.8, 12]} \quad (3)$$

where  $nCap[6, 12]$  and  $nCap[1.8, 12]$  are number of events with delayed energy in the range of [6MeV, 12MeV] and [1.8MeV, 12MeV] respectively. Energy leakage contributes to the combined efficiency obviously, to translate  $\epsilon_{Gd-combined}$  to the true Gd capture ratio  $\epsilon_{Gd}$ , one needs to correct for the energy leakage efficiency by

$$\epsilon_{Gd} = \frac{\epsilon_{Gd-combined} \cdot \epsilon_{1.8\text{MeV}}}{\epsilon_{6\text{MeV}}}, \quad (4)$$

where  $\epsilon_{6\text{MeV}}$  is the 6MeV cut efficiency nGd capture events,  $\epsilon_{1.8\text{MeV}}$  is the 1.8MeV cut efficiency for ALL nCap events. Both can be determined from MC. This method is in contrast to that used in the spallation nGd study described above.

TABLE III: AmC Results

	$\epsilon_{Gd-combined}$
AD1	$84.34\% \pm 0.12\%$
AD2	$84.62\% \pm 0.15\%$
AD1/2 combined.	$84.45\% \pm 0.10\%$

The accidental background for AmC, mainly for nH peak, is higher than the other two sources. The S/B ratio is  $\sim 2$  at nH peak. The results for AmC are shown in Table III.

Neutrons from AmBe source come from two states: ground state (G.S.) and first excited state (neutron emission correlated with a prompt 4.4MeV  $\gamma$ ) [8]. Kinetic energy of neutrons are both at  $\sim$ MeV level, except that G.S. neutrons are a little higher. The energetic G.S. neutrons can lose energy through proton recoil (PR) before finally get captured.  $\epsilon_{Gd-combined}$  obtained for G.S. PR and the prompt  $\gamma$  state agrees well (Table. IV). Hence we don't distinguish these two states and treat them as one combined data point.

TABLE IV: AmBe Results

	Ep	$\epsilon_{Gd-combined}$
AD1	G.S.	$84.62\% \pm 0.08\%$
	$\gamma$	$84.68\% \pm 0.07\%$
	all	$84.66\% \pm 0.05\%$
AD2	G.S.	$84.39\% \pm 0.14\%$
	$\gamma$	$84.76\% \pm 0.11\%$
	all	$84.55\% \pm 0.01\%$
AD1/2 combined	G.S.	$84.56\% \pm 0.07\%$
	$\gamma$	$84.70\% \pm 0.06\%$
	all	$84.63\% \pm 0.04\%$

The results for  $\epsilon_{Gd-combined}$  obtained with the PuC source are shown in Table V, three different neutron samples are tagged by various prompt energy range. PR and nC\* are both from G.S. neutrons. PR is the same as AmBe. nC\* represents neutrons inelastic scattering on C before finally captured on target. O\* denotes neutrons emitted together with a 6.13MeV  $\gamma$ . A significant discrepancy on  $\epsilon_{Gd-combined}$  between G.S. and the O\* state stands out. The major difference for these two states is the neutron energy. The G.S. neutrons have a kinetic energy distribution peaking at  $\sim$ 5MeV (the same level as AmC and AmBe neutrons), while the average energy of O\* state is much lower, at  $\sim$ 200keV [9]. Comparing the delayed spectra of G.S. with that of O\* state (Fig. 2), we can clearly see the nGd tail of G.S. is lower than that of O\* state, which is consistent with the larger  $\epsilon_{Gd-combined}$  value got for G.S.. To further understand this feature, we ran two sets of MC. One is a bare PuC source at detector center, the other uses the same configuration except with a realistic source package. As shown in Fig. 3, the discrepancy in leakage tail is reproduced in MC with source package added. In contrast, no visible difference can be seen in the case of bare source, which indicates the difference is caused by source package.

The source results are summarized in Table VI and compared with MC results. Data/MC are consistent within statistics for AmC and AmBe. As for PuC, discrepancy which can't be accounted for by statistics between data and MC exists. MC is systematically lower than data for all three neutron samples tagged by different prompt energy. We know MC is imperfect in several aspects:

1. The neutron energy in MC is off from data as indicated by the prompt energy distribution (Fig. 4).
2. The geometry of the source package is not well characterized, e.g. there might be some materials in real case but not known and coded in MC.

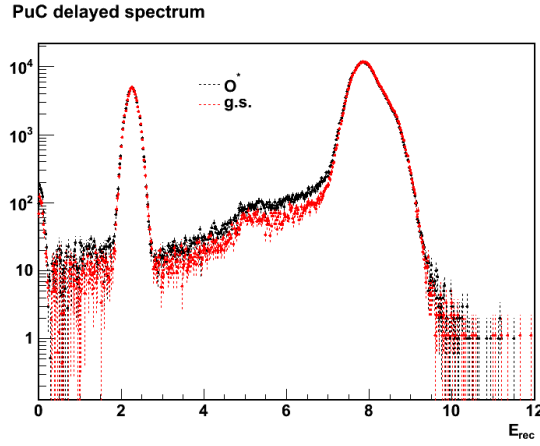


FIG. 2: Delayed spectra of PuC from different states in data.

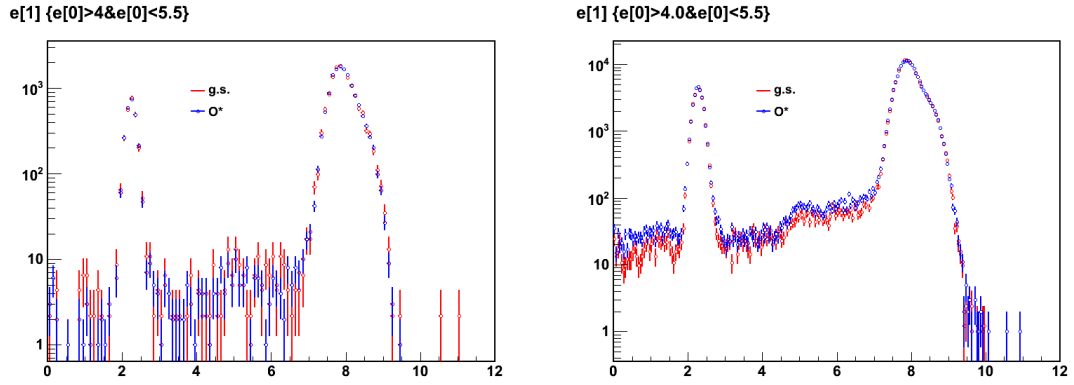


FIG. 3: Delayed spectra of PuC from different states in MC without (left) and with (right) the presence of the Manual Calibration System infrastructure.

TABLE V: PuC Results

	Ep	$\epsilon_{Gd-combined}$
AD1	PR	$84.69\% \pm 0.01\%$
	nC*	$84.67\% \pm 0.04\%$
	O*	$84.08\% \pm 0.03\%$
AD2	PR	$84.68\% \pm 0.01\%$
	nC*	$84.60\% \pm 0.02\%$
	O*	$84.17\% \pm 0.02\%$
AD1/2 combined	PR	$84.68\% \pm 0.01\%$
	nC*	$84.62\% \pm 0.02\%$
	O*	$84.14\% \pm 0.02\%$

Surely MC has room to be improved (e.g. tune neutron energy) to make data/MC match better. But for now, we propose to conservatively assign a 0.4% uncertainty to capture the biggest data/MC difference

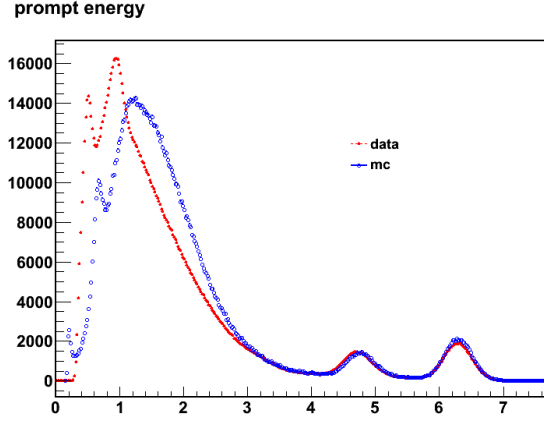


FIG. 4: Prompt spectra comparison of PuC between data and MC. The PR bulk clearly shifts to high energy in MC, indicating neutron energy distribution in MC is off from data.

(Fig. 5), which comes from the PuC results.

TABLE VI: Source results

		AmC	AmBe	PuC PR	PuC nC*	PuC O*
$\epsilon_{Gd-combined}$	Data	$84.45\% \pm 0.10\%$	$84.63\% \pm 0.04\%$	$84.68\% \pm 0.01\%$	$84.62\% \pm 0.02\%$	$84.14\% \pm 0.02\%$
	MC	$84.51\% \pm 0.12\%$	$84.47\% \pm 0.11\%$	$84.44\% \pm 0.03\%$	$84.21\% \pm 0.09\%$	$84.02\% \pm 0.08\%$

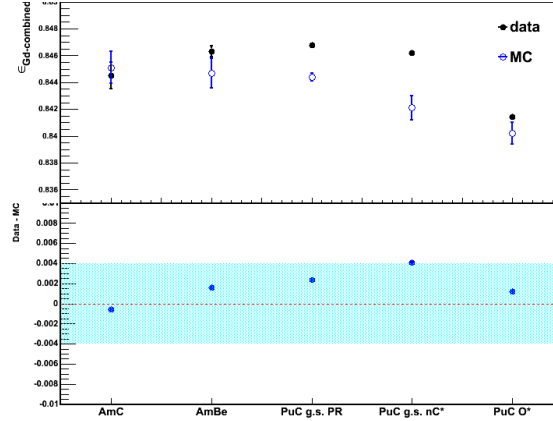


FIG. 5: All source results data vs MC. A 0.4% uncertainty band can cover the biggest difference between data and MC.

## 2. Central Value

There are two options to determine the central value of  $\epsilon_{Gd}$ . The first one is to obtain  $\epsilon_{Gd}$  directly from source data using Eq. 4 by taking into account the energy leakage efficiency.  $\epsilon_{6MeV}$  is calculated by taking

the reconstructed energy distribution of all the true nGd capture events identified by MC truth, and take the ratio of event number in  $[6\text{MeV}, 12\text{MeV}]$  over the total number of nGd capture events.  $\epsilon_{1.8\text{MeV}}$  is the same story but to take the reconstructed energy distribution of all neutron capture events identified by MC truth. Example distributions for AmC and AmBe are shown in Fig. 6. Table VII lists the  $\epsilon_{Gd}$  results after leakage correction for AmC and AmBe.

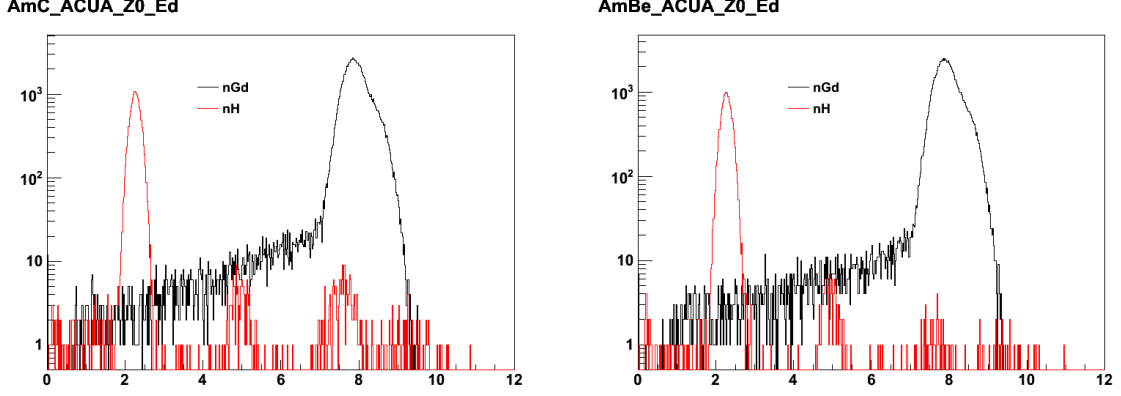


FIG. 6: Reconstructed energy distribution for neutron capture events based on MC for AmC (left) and AmBe (right) sources. Black line is for nGd capture events. Red line is for neutron capture events on any target except Gd.

TABLE VII:  $\epsilon_{Gd}$  for Sources

	AmC	AmBe
$\epsilon_{Gd-combined}$	$84.45\% \pm 0.10\%$	$84.63\% \pm 0.04\%$
$\epsilon_{6\text{MeV}}$	$0.985396 \pm 0.000381$	$0.987391 \pm 0.000369$
$\epsilon_{1.8\text{MeV}}$	$0.997932 \pm 0.000133$	$0.998273 \pm 0.000127$
$\epsilon_{Gd}$	$85.52\% \pm 0.10\%$	$85.56\% \pm 0.04\%$

### 3. Conclusion

In this note, we studied the Gd capture ratio by calculating the combined efficiency metric  $\epsilon_{Gd-combined}$  provided by various center-deployed special ACU sources and then correcting for leakage effects with special ACU MC. **Using this method, we obtain an AD-center Gd capture fraction of 85.5%, with an uncertainty of 0.4% that arises principally from differences between the data and the MC used to make the leakage correction.**

### C. H/Gd Ratio with MC

The AD-center Gd-capture fractions provided by spallation neutron and special ACU studies can be used to tune the Gd concentration in the Daya Bay MC, such that reported Gd capture fractions agree between data and MC. After this tuning, the AD-center H/Gd ratio for IBD MC is 85.7% [10].



### D. Summary

A number of independent data sets were used to determine the AD-center Gd capture fraction, which is determined largely by the Gd concentration in the Daya Bay ADs. **The AD-center Gd capture ratio is found to be 85.7%, with an uncertainty of 0.4% provided by both the spallation neutron and special ACU source studies.**

## IV. FULL-VOLUME GD CAPTURE FRACTION AND SPILL-OUT EFFECTS

The previous section concerned itself with finding the Gd capture fraction at the detector center, and matching this value between data and MC. In order to determine the Gd capture fraction for the entire target volume, which is the relevant number for the total absolute detection efficiency, one must take into account the proportion of IBD neutrons created in the GdLS that escape the target and capture outside the GdLS, where all captures are non-Gd. This process, termed the 'spill-out' effect, is naturally dependent on the proximity of the IBD interaction vertex to the edge of the GdLS.

The full-volume Gd capture fraction is determined mainly by the Daya Bay Monte Carlo. The accuracy and systematic uncertainty of this total Gd capture ratio reported by Monte Carlo simulation can be estimated by comparing total H/Gd ratios for existing non-IBD datasets between data and MC. Any consistent offset in full-volume Gd capture ratio between MC and various other datasets can be used to provide a corrected full-volume Gd capture ratio for the absolute efficiency analysis.

### A. Full-Volume nGd Fraction Using IBD MC

The tuned Monte Carlo is used to provide the full-volume Gd-capture fraction for the absolute analysis, since the true generated position and capture target of each IBD interaction is not known. This value is calculated using the M13B IBD Monte Carlo by counting the true number of IBD neutrons both generated and captured in the GdLS to the total number of events generated in the GdLS. This ratio is calculated to be 84.17%, with a statistical uncertainty of less than 0.1%. Variations in this ratio between differing ADs is expected to be  $<0.1\%$ .

### B. Full-Volume nGd Fraction Using MCS Data

Examining the nGd fraction of MCS data and MC is a good way to benchmark the ability of the MC to provide an accurate full-volume Gd capture ratio for IBD [11]. The entire MCS dataset was analyzed for the purposes of this study, along with the entirety of the MCS MC dataset. In these dataset, event pairs with time difference within  $[1, 200]$  us are regarded as signals, while event pairs with time difference within  $[201, 400]$  us is regarded as backgrounds. The prompt energy cut is  $[0.3, 12]$  MeV, the delayed energy cut is  $[0.3, 12]$  MeV, so that the nH peak is visible in the delayed spectrum. Off-time-window background subtraction is used to subtract backgrounds. To correct for residual differences in energy scales between data and MC, the MC energy scale at each position is scaled by a constant so that the nGd peak energy matches that of the data. This scaled background-subtracted delayed spectrum is used to calculate the nGd capture ratio.

The nGd fraction is defined as the number of nGd capture event divided by the sum of nH capture events and nGd capture events, where the number of nGd(nH) capture events is the integral of the fitted function for nGd(nH) peak in delayed spectrum. For this study, we utilize the same  $\epsilon_{Gd-H}$  metric used in the spallation neutron AD-center Gd capture fraction study.

Figure 7 shows  $\epsilon_{Gd-H}$  values versus MCS Z-position. Figure 8 shows the same result for the Z dependence, at different radii. The MC agrees with data well at most part of the detector. The difference between data and MC becomes larger when the source is close to the boundary of the IAV.

The target-wide  $\epsilon_{Gd-H}$  values provided in these figures for MCS real data and MC data can be used to obtain a full-volume nGd fraction. Figure 9 shows all the MCS MC points simulated. The red points are

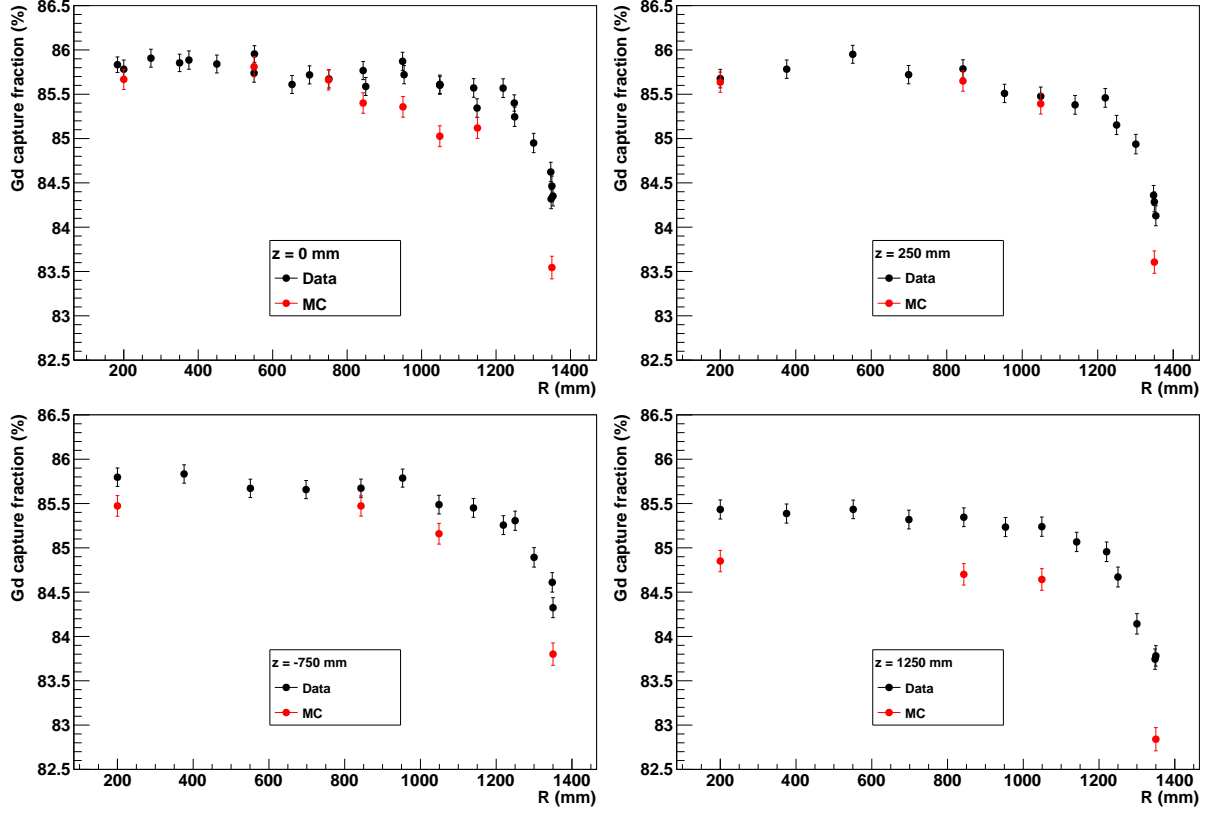


FIG. 7: nGd fraction comparison along the radial direction at different Z value between data (black), MC (red). The four figures (left to right, top to bottom) correspond to Z values equal to 0, 250, -750 and 1250 mm. Only statistical errors are included in the plots, the systematic errors are estimated to be 0.2% due to background subtraction and energy scale difference between data and MC.

selected to obtain the Z and R dependence of the nGd fraction,  $R(r)$  and  $Z(z)$ . Similar points are chosen to determine the full-volume nGd fraction in data.

The R dependence for both data and MC are fitted with a constant for  $R < 750$  mm, and a polynomial of order 4 for  $R > 750$  mm, the two functions are connected at  $R = 750$  mm. The Z dependence for data and MC are fitted with polynomial of order 7 and 8, respectively. The result of the fitting is showing in Fig 10.

The functions are then integrated over the target volume to obtain the combined nGd fraction. The uncertainty of the result is propagated through the errors of the parameters of the fitted function.

$$\text{nGd fraction} = \frac{R(r)Z(z)rdrdzd\phi}{\text{target volume}} \quad (5)$$

The resulting full-volume Gd capture fractions are shown in Table VIII. The statistical uncertainties on these values are roughly 0.2%. The absolute value of the data-based full-volume Gd capture ratio should be treated carefully: the presence of the MCS source infrastructure and the higher neutron energies of the PuC mean that the MCS-reported Gd capture fraction should not be used as a proxy for the IBD Gd capture fraction.

That said, comparisons of the MCS PuC Gd capture fractions between MC and data can provide a substantive benchmark as to how precisely the MC can predict full-volume Gd capture ratios. This benchmark can then serve as a guide to defining systematics on this ratio for IBD neutrons. For the MCS, a 0.6%

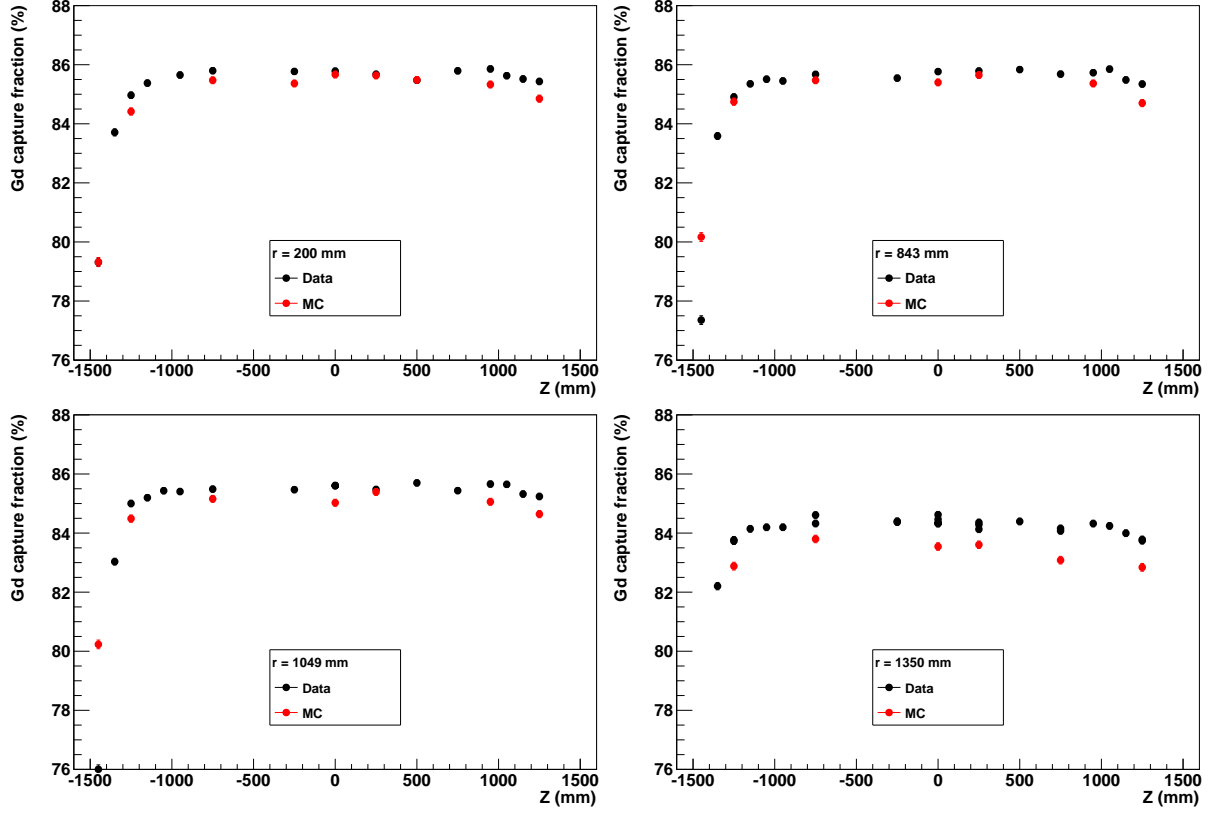


FIG. 8: nGd fraction comparison along the Z direction at different radius between data (black), MC (red). The four figures (left to right, top to bottom) correspond to radius 200, 843, 1049 and 1350 mm. Only statistical errors are included in the plots, the systematic errors are estimated to be 0.2% due to background subtraction and energy scale difference between data and MC.

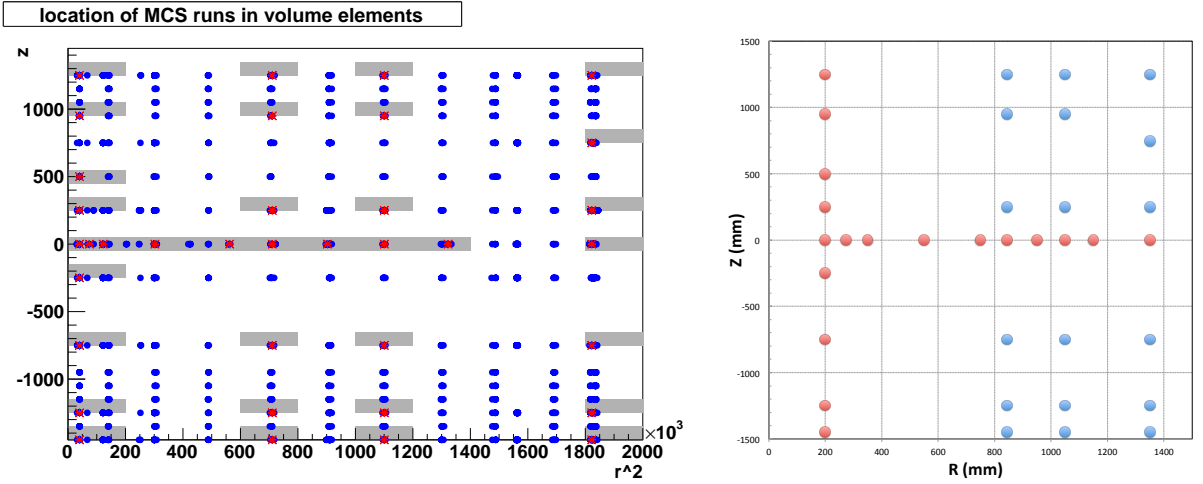


FIG. 9: Left: The positions of the MCS data (blue) and MC (red) points. The volume elements are defined to give good coverage, but do not line up perfectly between data and MC. Right: The red points are used to obtain the Z and R dependence of the nGd fraction.

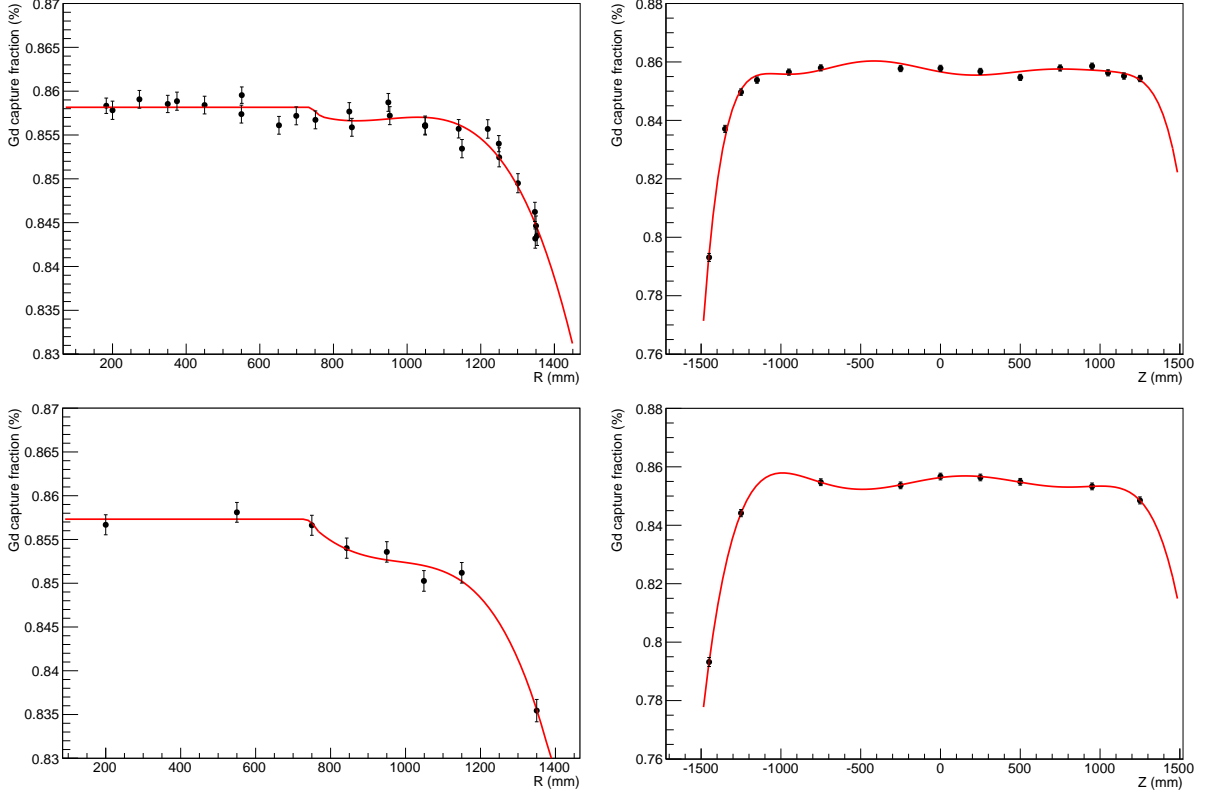


FIG. 10: The fitted functions for R and Z dependences of nGd fraction for data (upper 2 figures) and MC (lower 2 figures).

discrepancy in Gd capture fraction exists between Monte Carlo and data. One can clearly see in Figures 7 and 8 the systematic shifts in  $\epsilon_{Gd-H}$  between data and MC, so an integrated offset in full-volume Gd capture fraction between data and MC should not be surprising. **This 0.6% difference between Monte Carlo and data can serve as the systematic uncertainty in the MC-reported IBD full-volume Gd capture fraction.**

TABLE VIII:

	Gd fraction	Statistical Uncertainty
data	84.1%	0.5%
MC	83.5%	0.5%

The MC-data difference was also investigated while including alterations to the data selection and fitting. To account for the uncertainty in  $\epsilon_{Gd-H}$  because of the lack of data or MC at high Z, the  $\epsilon_{Gd-H}$  for these positions was altered to mirror that at low Z. This alteration causes a 0.5% alteration in the Gd capture fraction for both MC and data. Other differing fitting functions produce differing Gd capture fractions on the order of 0.5%, allowing us to place a systematic uncertainty of 0.5% on these Gd capture fraction values. If full-volume Gd capture fractions are calculated separately for the three different PuC peak types (proton-recoil, nC\* and O\*), all resulting fractions agree within 0.6% between MC and data. This provides confidence that MC predictions of this fraction are equally precise over a broad range of neutron energies.

### C. Full-Volume nGd Fraction Using MCS Data, An Independent Check

Another independent comparing the extracted full-volume nGd fraction using MCS data/MC has been done, using a different MCS coincidence pair selection, background subtraction and fitting method. The analysis method is the same as that described in Section III B. After getting the background subtracted delayed spectrum for each MCS deployment position,  $\epsilon_{Gd-H}$  and  $\epsilon_{Gd-combined}$  can be calculated respectively. Note that they were calculated by simply summing up the bin entries within certain energy region, instead of by integrating over the fitted function on delayed energy peaks as in above analysis. The full MCS data and MC dataset were analyzed. And only common vertex existed in both data and MC are used to build the spill-out model. Then the same procedures went for data and MC until the full-volume Gd-capture fraction was obtained.

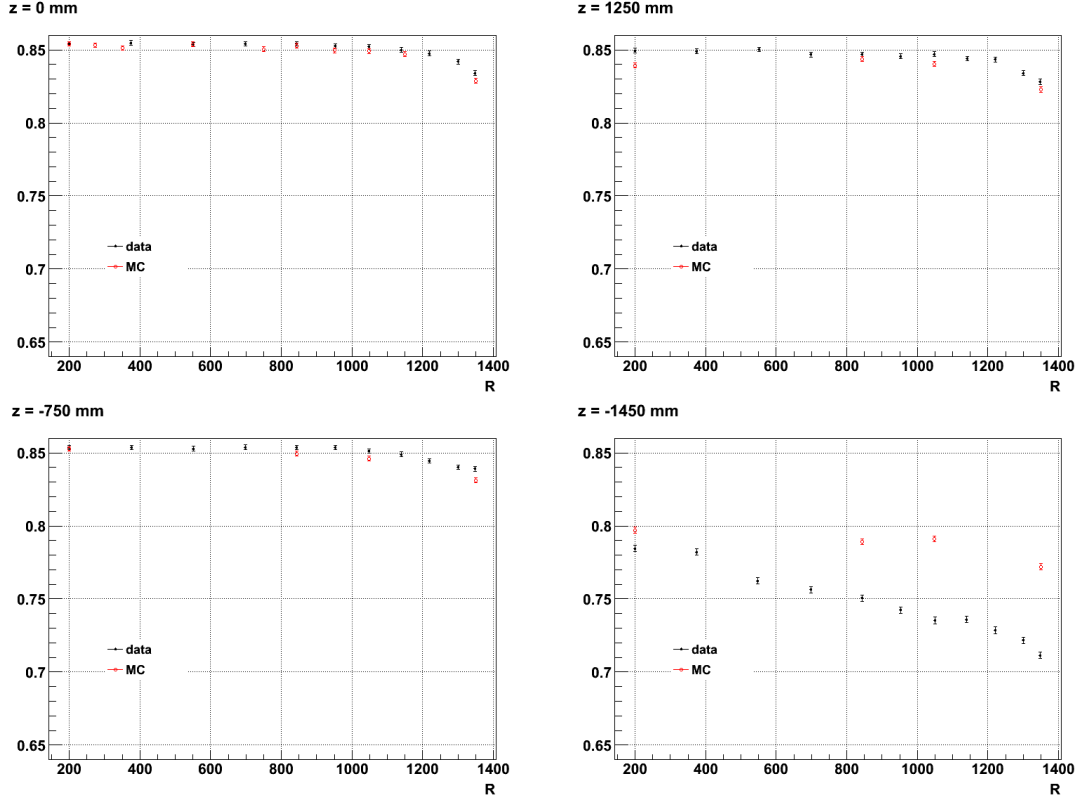
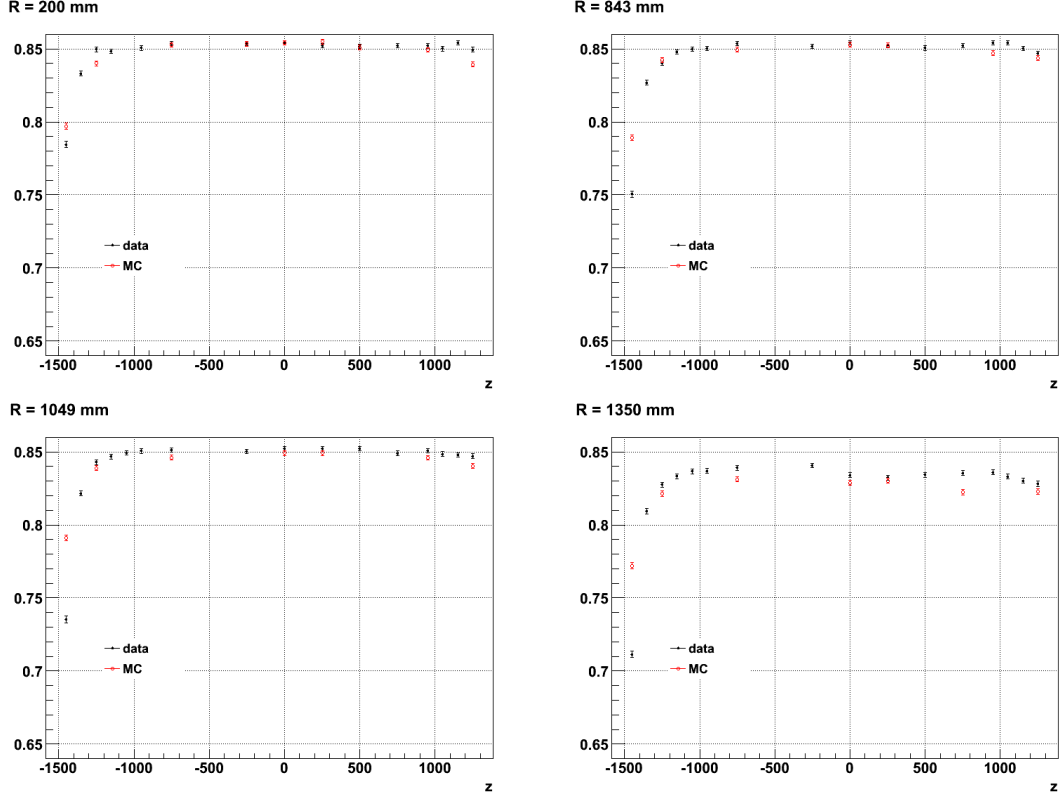


FIG. 11:  $\epsilon_{Gd-H}$  R-dependence for data/MC

Figs. 11 and 12 shows R-, Z-dependence from data and MC. R-, Z-dependence were assumed to be independent and the functional form used to fit the R-, Z-dependence was shown in Eq. 6, 7. R direction employed the same functional form as that for  $Z > 0$ . Z-dependence functional form is almost symmetric between  $Z > 0$  and  $Z < 0$  except we still want to allow an up-down asymmetry, which means the parameters controlling the falling slope towards edge (i.e.  $p_1, p_4$ ) were not constrained to be the same.

$$f(z) = \begin{cases} \frac{p_0}{1 + (\frac{p_0}{p_1} - 1)e^{-p_2(-z+p_3)}} & , z > 0 \\ \frac{p_0}{1 + (\frac{p_0}{p_4} - 1)e^{-p_2(z+p_3)}} & , z \leq 0 \end{cases} \quad (6)$$

$$f(r) = \frac{p_0}{1 + (\frac{p_0}{p_1} - 1)e^{-p_2(-r+p_3)}} \quad (7)$$

FIG. 12:  $\epsilon_{Gd-H}$  Z-dependence for data/MC

The parameters can be understood as following:  $p_0$ , center Gd capture fraction;  $p_1, p_4$  Gd capture fraction at the edge;  $p_2$ , falling slope of spill-out towards edge;  $p_3$ , radius of IAV boundary.

Fig. 13 shows the fits for  $R(Z = 0), Z(R = 200\text{cm})$  center points. The fit to both data and MC is pretty good. The full-volume nGd fraction is calculated using Eq. 5. To study the possible systematics arising from the model as well as the fitting range, we tried to constrain the Z-dependence to be symmetric and varies the integration window for the full-volume results. The largest difference between data and MC is 0.3%. To make the most of MCS data, we also tried to include all reasonable data points in fitting the R-, Z-dependence, namely, the off-center data points. They were normalized to the center ratio before fits were performed. The full-volume ratio were summarized in Table. IX. The biggest difference between data and MC is 0.7%, which confirms the results from above analysis.

TABLE IX: Full-volume  $\epsilon_{Gd-H}$  results. "Fixed" means the full-volume integral window is a fixed window  $[-1550, 1550]$  for Z and  $[0, 1550]$  for R; "Float" means the full-volume integral window depends on the fitting results, i.e.  $[-p_3, p_3]$  for z and  $[0, p_3]$  for R. Asymmetric(Symmetric) denotes whether up-down Z-dependence asymmetry is allowed or not.

	Data	MC	Diff.
Fixed, Asymmetric	83.76%	84.31%	0.5%
Float, Asymmetric	83.57%	83.70%	0.1%
Fixed, Symmetric	83.57%	84.27%	0.7%
Float, Symmetric	83.44%	83.63%	0.2%

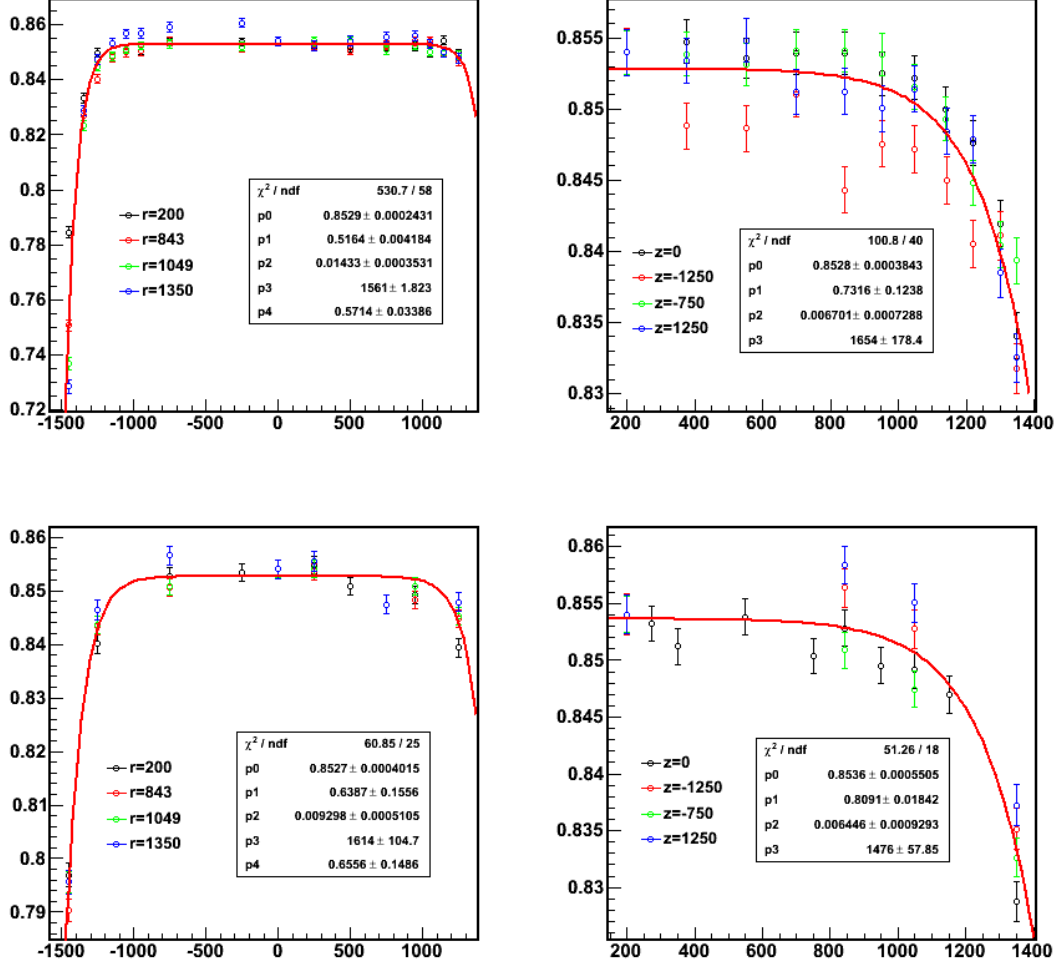


FIG. 13: Fit for  $\epsilon_{Gd-H}$ . Upper(bottom) two plots for data(MC), left(right) two plots for Z-(R-) dependence.

#### D. Summary

To summarize, the full-volume Gd capture fraction is calculated to be 84.17% using M13B IBD Monte Carlo. The uncertainty on this value, 0.7%, comes from the maximum difference in Gd capture fractions calculated between MCS full-volume PuC data and Monte Carlo. If this uncertainty is combined with that from the uncorrelated AD-center Gd capture ratio (0.4%), we obtain a total Gd capture fraction uncertainty of 0.8%.

#### V. GD CAPTURE DETECTION EFFICIENCY

Of the total target IBD interactions capturing on Gd, a small percentage in the tail of this energy distribution will have a delayed reconstructed energy below the 6 MeV delayed energy cut. This inefficiency arises as a major portion of gammas from some Gd captures exit the scintillating region of the detector

before depositing their energy. In order to properly estimate the predicted absolute flux, this Gd capture detection efficiency must be properly estimated.

### A. IBD Tail Shape MC/Data Comparison

In order to obtain a constrained and more reliable value for the 6 MeV cut efficiency from MC, one can compare IBD tail shapes directly between data and MC [13]. Delayed energy tail shapes in Monte Carlo are highly dependent on the modelling of the energy spectrum of gammas released after the capture of a neutron by  $^{157}\text{Gd}$  and  $^{155}\text{Gd}$ . The Gd gamma model used for the 2012 PRL paper, shown in Figure ?? is based on those given in Nuclear Data Table A5 (1968). For this paper, a number of other models were prepared [14, 15]. One model, shown in the right panel of Figure ??, is based on the default Geant4 Gd gammas spectrum, but altered to ensure total energy conservation and to remove non-physical high-energy gammas. Another model, shown in the center of Figure ?? is derived directly from Gd gamma measurements made at Caltech using an HPGe detector [12].

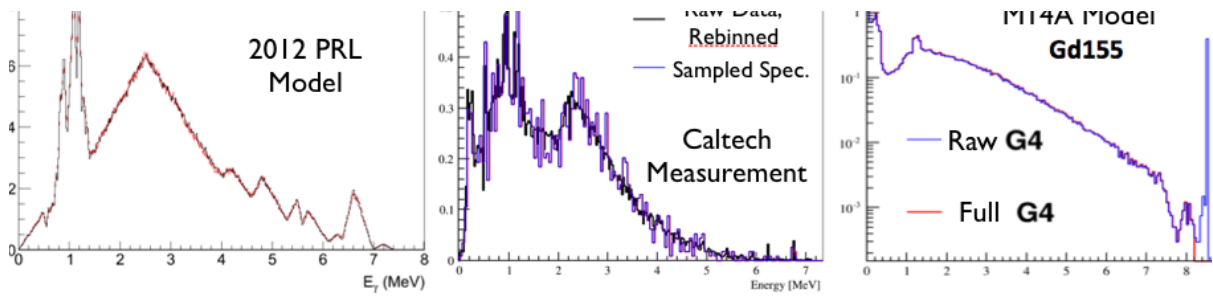


FIG. 14: Data/MC ratios for each individual energy bin before and after correction. A linear correction,  $N_{new,lin}$  is shown on the left, while a quadratic correction,  $N_{new,quad}$ , is shown on the right.

Figure 15 shows the comparison between the background-subtracted IBD delayed spectrum summed between the Daya Bay near sites in data and MC including the two newly-derived Gd gamma models (M14A for the G4-based model, and a special M13B-era MC dataset generated by Guofu for the Caltech model). Identical selection cuts from the PRL IBD analysis are used, except that the low-energy prompt energy cut is tightened from 0.7 to 3.5 MeV to ensure a high-purity sample of inverse beta decays. To further ensure purity of IBD nGd captures in the data sample, the spectrum of accidental backgrounds is removed by normalizing the low-energy singles spectrum of these detectors to that of the delayed IBD spectrum and subtracting. Any remaining backgrounds from AmC or He/Li are small contributions, and will provide nearly the same delayed spectrum as that of IBD.

One can see relatively good agreement in tail shape between data and the Monte Carlo data utilizing these new nGd gamma spectrum models. To more quantitatively describe the data/MC agreement, we define a tail shape metric:

$$R_{ts} = \frac{N(3 - 6\text{MeV})}{N(3 - 12\text{MeV})}. \quad (8)$$

In order to provide a proper comparison between data and Monte Carlo, all Monte Carlo spectra are scaled in energy to provide an identical nGd peak location as the data (7.937 MeV for the lower-energy  $^{157}\text{Gd}$  peak). After energy scaling,  $R_{ts}$  ratios can be seen in Table ??; the ratio for data is 7.02%, while it is MC it is 6.97% for M14A and 6.91% for the Caltech-based MC, with statistical uncertainties on data and MC of less than 0.1%. Agreement in this energy range is in the vicinity of 0.1%. Altering the normalization of the subtracted accidental background within reasonable bounds provides negligible change ( $<0.1\%$ ) to  $R_{ts}$  in data.



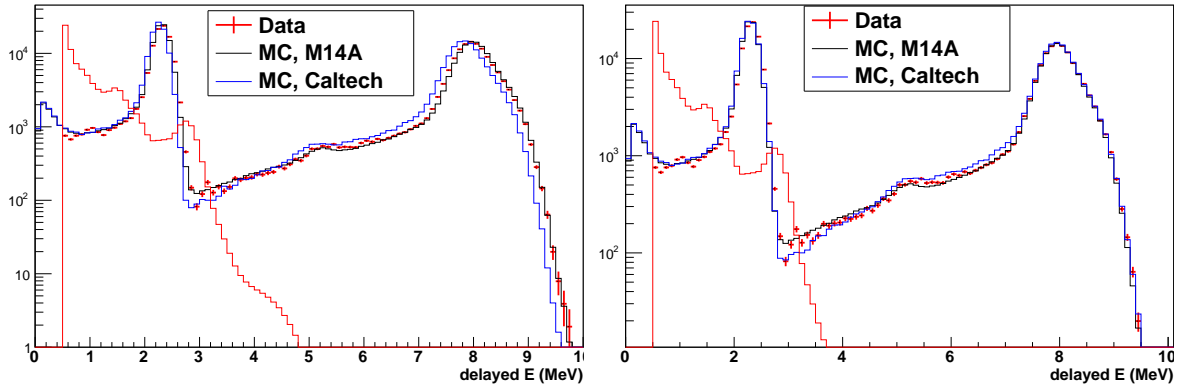


FIG. 15: Left: comparison of background-subtracted delayed signal shapes of the near-site ADs between data and uncorrected MC. One can see a clear over-estimation of nGd tail shape comparing MC to data. Right: same comparison between data and corrected MC. One can also see offsets between the nC and nH peaks in data and MC, which are discussed further in the text.

Dataset	$R_{ts}$ (%)	$R_{<3MeV}$ (%)	$\epsilon_{tail}$ (%)
Data	7.02	-	-
2012 PRL MC [13]	7.9	1.2	92.3
M14A	6.97	0.96	92.9
Caltech MC	6.91	0.45	92.9

TABLE X: Calculated 6 MeV nGd cut efficiencies and tail shape ratios  $R_{ts}$  for various datasets. MC datasets differ primarily in that they utilize differing Gd gamma spectrum modelling.

There are a number of interesting differences to be noted between tail shapes between MC data the data. In particular, it appears that the Caltech MC does a poor job in reproducing the tail shape of the data at the low end of this energy range, indicating that it will do a worse job than the M14A G4-based model at properly predicting the proportion of nGd tail events below 3 MeV, where the true proportion in data is obscured by the large nH capture peak. For this reason, the M14A G4-based model is chosen to provide the official estimate of the nGd detection efficiency, while the Caltech-based MC data serves as a data-based cross-check on this value and its assigned uncertainties. In contrast to the agreement between data and the new MC modelling, the 2012 PRL MC data differs in  $R_{ts}$  by 0.9%; this indicates the bad fit of this particular nGd gamma model to the data, and that this model should not be used to estimate the nGd detection efficiency uncertainty.

After choosing the G4-based M14A MC as a benchmark, the predicted absolute nGd detection efficiency can be calculated by applying the full array of standard IBD analysis cuts to all nGd-captured IBDs in the M14A data. After providing a similar energy scaling described above to match the data and MC energy scale, **the total percentage of nGd IBD above the 6 MeV cut threshold is determined to be 92.7%.**

A large uncertainty in this estimate originates from the fact that a data-MC comparison does not exist for nGd of less than 3 MeV, as this region is obscured by the nH capture peak. We conservatively assign a 100% uncertainty to the fractional contribution to the total nGd from this region,  $R_{<3MeV}$ , of 0.9%, as shown in Table X. The data-based Caltech MC has a  $R_{<3MeV}$  of 0.45%, providing a good cross-check of this uncertainty contribution.

Another complicating factor is introduced by the possibility of energy scale shifts between differing data types. One can see in Figure 15 that when the nGd peaks align between MC and data, the nH and nC peaks at roughly 2.2 and 4.9 MeV are shifted by approximately 1.4%. This relative difference in peaks between data and MC likely arise from a differing non-linearity and residual non-uniformity in MC and data. For

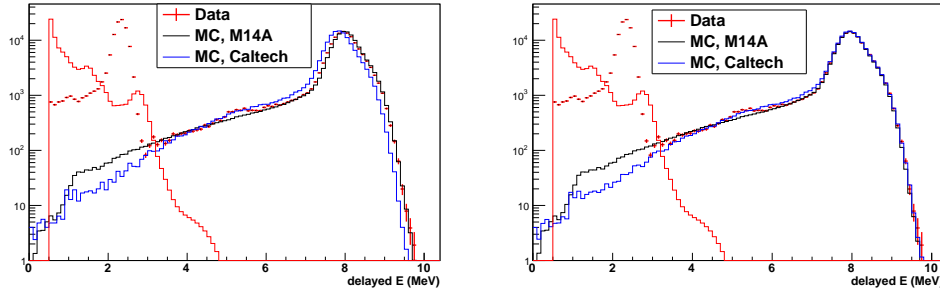


FIG. 16: Data/MC tail shape comparison for each individual energy bins using only nGd captures from the Caltech-based MC and the Geant4-based M14A MC. MC spectra are shown without (left) and with (right) energy scaling to match with data.

non-uniformity, this can be confirmed by adding cuts on reconstructed position: If events reconstructed in the LS are excluded, the relative shift between nH peaks between data and MC reduces from 1.4% to around 1%. In the same way that nGd and nH peaks are shifted differently between data and MC, so can the nGd tail can also be shifted differently with respect to the nGd peak, since nGd tail events are distributed closer to the edges of the GdLS. The change in uncorrected  $R_{ts}$  associated with a 1% shift in the nGd tail is 0.2%, which can be used as an estimate of the uncertainty in agreement between data and MC  $R_{ts}$  arising from non-uniformity disagreements. Other smaller associated uncertainties in the total efficiency estimate arise from statistics (0.1%), accidental background-subtraction (0.1%)

In summary, in order to obtain a reasonable true 6 MeV nGd cut efficiency from MC, a new nGd capture gamma model has been included in the default Monte Carlo that better reproduces the nGd tail shape in data. **With uncertainty contributions from MC-data differences in tail shape above 3 MeV (0.1%), statistics (0.1%), background subtraction (<0.1%), non-uniformity effect uncertainties (0.3%) and lack of constraint on low-energy regions (0.9%), a corrected 6 MeV cut efficiency of  $92.7\% \pm 0.9\%$  is calculated.**

## B. MCS Tail Shape Studies

One of the most important functions of the Manual Calibration System (MCS) is validation of the Daya Bay Monte-Carlo. One metric for comparison between data and Monte-Carlo is the shape of the low-energy tail of the neutron-gadolinium capture gamma rays. Signal selection in this study is essentially identical to that performed in the MCS full-volume Gd capture fraction study. After applying cuts, two primary histograms are produced for further analysis, one containing signal events and the other containing off-time-window backgrounds (Fig. 17) [22].

Most of the PuC nGd captures do not have an associated prompt event (see DocDB 8301 for rates). Due to the high neutron rate produced by the source, pileup of uncorrelated nGd-nGd events is observed at 8 MeV in the prompt and delayed spectra. These uncorrelated events are removed by off-time-window subtraction (Fig 17). The background dt window is chosen between 200-299.5 microseconds, due to an upswing in large dt events at the nGd-nGd peak. This peak is present in data and Monte-Carlo and is seen in two independent analysis codes (Fig. 18).

Three regions of the prompt spectrum are chosen to study the nGd tail shape vs. neutron energy. These three regions are shown in Fig. 19. The prompt spectrum was derived by integrating the delayed events in Fig. 17 from 4-12 MeV.

After fitting the prompt spectrum to define the nC and O\* Evis energies, three delayed energy spectra are obtained for the low-energy (0.7-3.5 MeV), nC (4.4 MeV), and O\* (6 MeV) prompt energy regions, respectively (Fig. 20). To study the nGd tail shape, three integration regions are defined: 1.8-12 MeV, 3.25-6 MeV, and 6-12 MeV. The ratio (6-12 MeV)/(1.8-12 MeV) is identical to the  $\epsilon_{Gd,combined}$  metric used

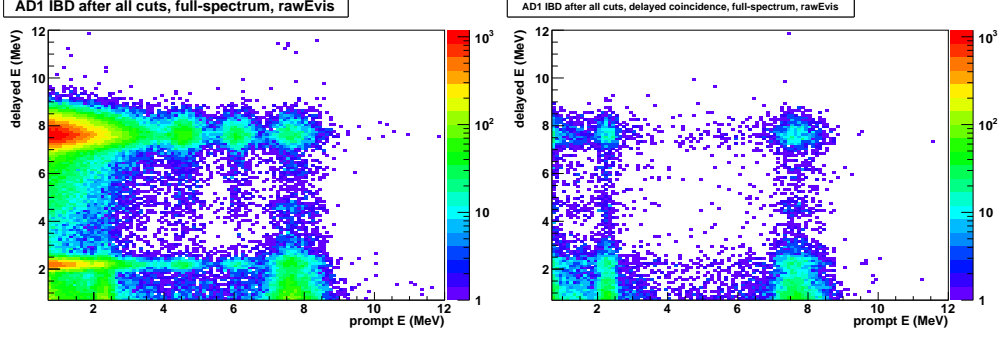


FIG. 17: IBD-like PuC events in the signal (left,  $1 < dt < 200$ ) and background (right,  $200 < dt < 299.5$ ) regions.

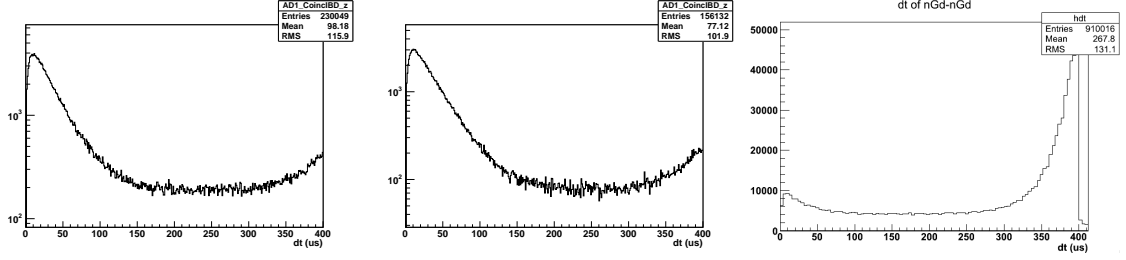


FIG. 18: Time difference between prompt and delayed events for data (left), Monte-Carlo (center), and data using a different analysis code and energy cuts to select the nGd-nGd energy peak (right). The exponential rise has lifetime consistent with the nGd capture time. An off-time-window region of 200-299.5 is chosen for background subtraction.

in the AD-center special ACU study and is roughly equivalent to the combined neutron detection efficiency from all sources. The ratio (3.25-6 MeV)/(3.25-12 MeV) is representative of the inefficiency of the 6 MeV cut for nGd captures. The lower bound of these integrals is determined by a fit to the nGd peak of the Evis spectrum. As seen in Fig. 20, the uncertainty of the fit to the 7.937 MeV isotope of the nGd capture peak is negligible. The uncertainty on the integral from the uncertainty of the integration range is much smaller than the statistical uncertainty.

After integrating each range (1.8-12 MeV, 3.25-12 MeV, 6-12 MeV) of each of delayed spectrum (LE, nC, O\*), the ratios (6-12 MeV)/(1.8-12 MeV) and (3.25-6 MeV)/(3.25-12 MeV) are formed. Care is taken to compute the uncertainties of these ratios correctly, since the regions are subsets of each other. We define  $a$  as the counts in the smaller region,  $c$  as the counts the larger region (which includes  $a$ ), and region  $b = c - a$ . The statistical uncertainty on  $R = a/c = a/(a + b)$  is computed as

$$(\delta R)^2 = \left( \frac{\partial R}{\partial a} \right)^2 (\delta a)^2 + \left( \frac{\partial R}{\partial b} \right)^2 (\delta b)^2 \quad (9)$$

$$= \left( \frac{1}{a+b} + \frac{-a}{(a+b)^2} \right)^2 (\delta a)^2 + \left( \frac{-a}{(a+b)^2} \right)^2 (\delta b)^2 \quad (10)$$

$$= \left( \frac{b}{(a+b)^2} \right)^2 (\delta a)^2 + \left( \frac{a}{(a+b)^2} \right)^2 (\delta b)^2 \quad (11)$$

$$(\delta R)^2 = \frac{b^2 (\delta a)^2}{c^4} + \frac{a^2 (\delta b)^2}{c^4} \quad (12)$$

$$(13)$$

These ratios are shown vs.  $r^2$  and  $z$  volume elements for Monte-Carlo and data in Figs. 21, 22, and 23. Since the number of MC simulated locations are fewer than the number of data runs, Figs. 22 and 23

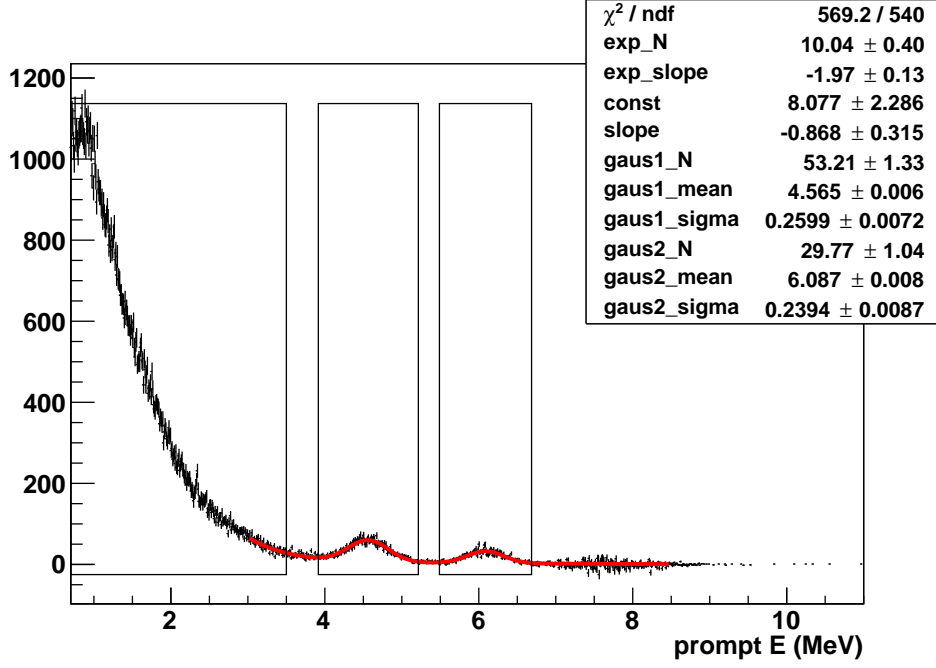


FIG. 19: Prompt events, where the delayed energy is 4-10 MeV. The fit function is the sum of an exponential, a linear function, and two Gaussian distributions. Three ranges, denoted by boxes, are used to derive three delayed spectra for tail shape studies (Fig. 20). The first region is 0.7-3.5 MeV. The second and third regions are defined as the Gaussian mean  $\pm 2.5\sigma$ .

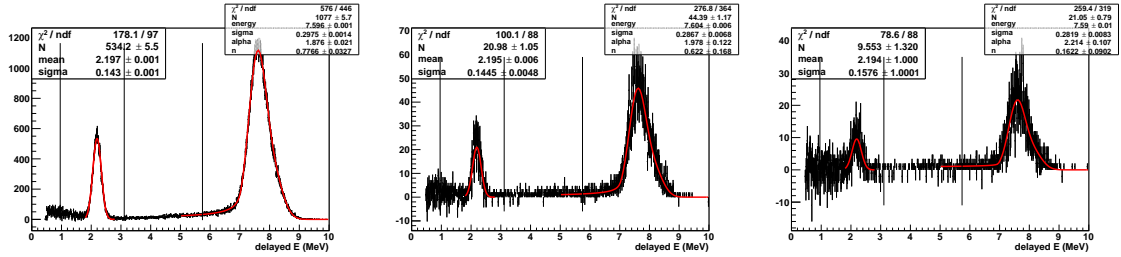


FIG. 20: Three delayed Evis spectra, obtained by integrating the three distinct prompt energy regions: 0.7-3.5 MeV (left), the 4.4 MeV prompt peak (center), and the 6 MeV prompt peak (right). For the tail shape studies, integration regions are defined from 1.8-12 MeV, 3.25-12 MeV, and 6-12 MeV. The lower edge of these integration regions are determined by a double crystal ball fit to the 8 MeV nGd capture peak.

restrict the analyzed data points to be located at the same positions as the MC points, within 10 mm in  $r$  and 1 mm in  $z$ . The volume elements are integrated over  $\phi$ .

The overall consistency between data and Monte-Carlo tail shapes can be derived by comparing the histograms in Figs. 22 and 23. The difference between data and MC ratios is shown in Fig. 24, and differences between prompt energies cuts are shown in Fig. 25.

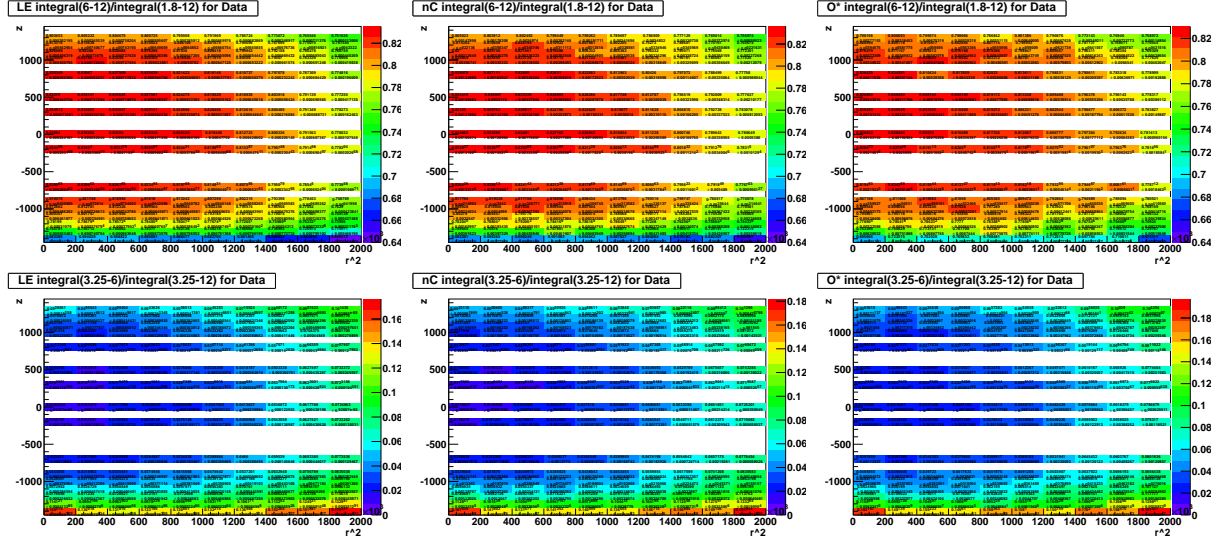


FIG. 21: Tail shape ratios for MCS data. The top row shows the ratio (6-12 MeV)/(1.8-12 MeV) and the bottom row shows the ratio (3.25-6 MeV)/(3.25-12 MeV). Three prompt integration windows: 0.7-3.5 MeV, the nC peak, and the O\* peak are given in the left, center, and right columns, respectively.

TABLE XI: Tail shape ratios for MCS data, averages for Fig. 21. The top two rows show the weighted averages of all entries. The second two rows show the same, but using unweighted averages (i.e. assuming all volume elements have the weight=1).

	Low Energy prompts	nC peak	O* peak
(6-12 MeV)/(1.8-12 MeV)	$0.78392 \pm 0.00003$	$0.79018 \pm 0.00016$	$0.79300 \pm 0.00028$
(3.25-6 MeV)/(3.25-12 MeV)	$0.05584 \pm 0.00002$	$0.05125 \pm 0.00009$	$0.05562 \pm 0.00016$
(6-12)/(1.8-12)	$0.79176 \pm 0.07906$	$0.79282 \pm 0.07906$	$0.79182 \pm 0.07906$
(3.25-6)/(3.25-12)	$0.06017 \pm 0.07906$	$0.06051 \pm 0.07906$	$0.06505 \pm 0.07906$

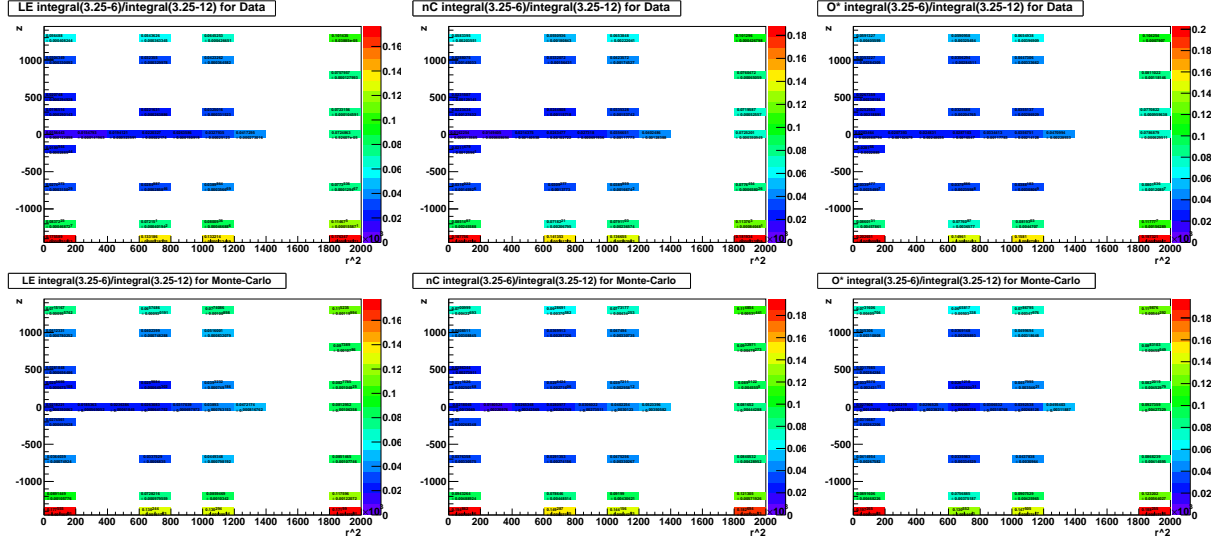


FIG. 22: Tail shape ratio  $(3.25-6 \text{ MeV})/(3.25-12 \text{ MeV})$  for MCS data and Monte-Carlo. The top row shows the ratio for data and the bottom row shows the ratio for Monte-Carlo. Three prompt integration windows: 0.7-3.5 MeV, the nC peak, and the O\* peak are given in the left, center, and right columns, respectively.

TABLE XII: Tail shape ratio  $(3.25-6 \text{ MeV})/(3.25-12 \text{ MeV})$ , averages for Fig. 22. The top two rows show the weighted averages of all entries. The second two rows show the weighted averages excluding volumes at  $z = 0$  and  $r = (300, 500, 900, 1300)$  to give a more uniform distribution of samples. The fifth through eighth rows show the same, but using unweighted averages (i.e. assuming all volume elements have the weight=1).

	Low Energy prompts		nC peak	O* peak
Data	0.06970 $\pm$ 0.00003	0.06412 $\pm$ 0.00015	0.06862 $\pm$ 0.00027	
Monte-Carlo	0.04482 $\pm$ 0.00013	0.04348 $\pm$ 0.00054	0.04768 $\pm$ 0.00054	
Data	0.07551 $\pm$ 0.00003	0.07061 $\pm$ 0.00016	0.07580 $\pm$ 0.00030	
Monte-Carlo	0.04826 $\pm$ 0.00015	0.04668 $\pm$ 0.00059	0.05097 $\pm$ 0.00059	
Data	0.05974 $\pm$ 0.17150	0.06137 $\pm$ 0.17150	0.06652 $\pm$ 0.17150	
Monte-Carlo	0.06603 $\pm$ 0.17150	0.06904 $\pm$ 0.17150	0.06989 $\pm$ 0.17150	
Data	0.06428 $\pm$ 0.18257	0.06609 $\pm$ 0.18257	0.07118 $\pm$ 0.18257	
Monte-Carlo	0.07080 $\pm$ 0.18257	0.07399 $\pm$ 0.18257	0.07480 $\pm$ 0.18257	

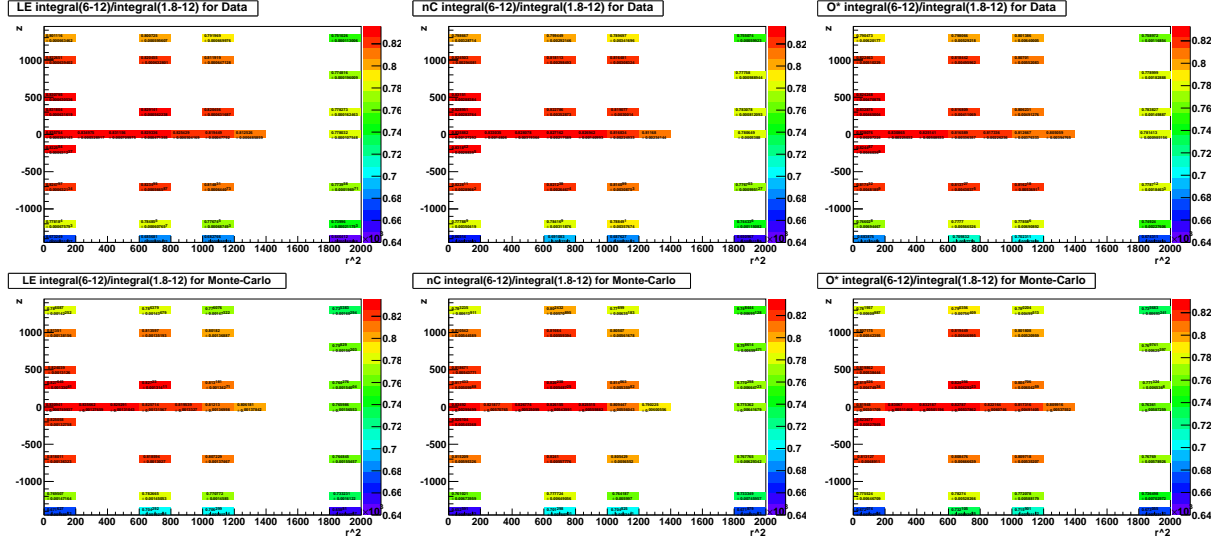


FIG. 23: Tail shape ratio (6-12 MeV)/(1.8-12 MeV) for MCS data and Monte-Carlo. The top row shows the ratio for Data and the bottom row shows the ratio for Monte-Carlo. Three prompt integration windows: 0.7-3.5 MeV, the nC peak, and the O\* peak are given in the left, center, and right columns, respectively.

TABLE XIII: Tail shape ratio (6-12 MeV)/(1.8-12 MeV), averages for Fig. 23. The top two rows show the weighted averages of all entries. The second two rows show the weighted averages excluding volumes at  $z = 0$  and  $r = (300, 500, 900, 1300)$  to give a more uniform distribution of samples. The fifth through eighth rows show the same, but using unweighted averages (i.e. assuming all volume elements have the weight=1).

	Low Energy prompts nC peak		O* peak
Data	0.76669 $\pm$ 0.00005	0.77450 $\pm$ 0.00025	0.78034 $\pm$ 0.00045
Monte-Carlo	0.79664 $\pm$ 0.00024	0.79801 $\pm$ 0.00099	0.79561 $\pm$ 0.00096
Data	0.76253 $\pm$ 0.00005	0.77009 $\pm$ 0.00026	0.77565 $\pm$ 0.00048
Monte-Carlo	0.79267 $\pm$ 0.00026	0.79526 $\pm$ 0.00106	0.79140 $\pm$ 0.00102
Data	0.79027 $\pm$ 0.17150	0.79064 $\pm$ 0.17150	0.78969 $\pm$ 0.17150
Monte-Carlo	0.78482 $\pm$ 0.17150	0.78431 $\pm$ 0.17150	0.78623 $\pm$ 0.17150
Data	0.78551 $\pm$ 0.18257	0.78606 $\pm$ 0.18257	0.78570 $\pm$ 0.18257
Monte-Carlo	0.77977 $\pm$ 0.18257	0.78007 $\pm$ 0.18257	0.78123 $\pm$ 0.18257

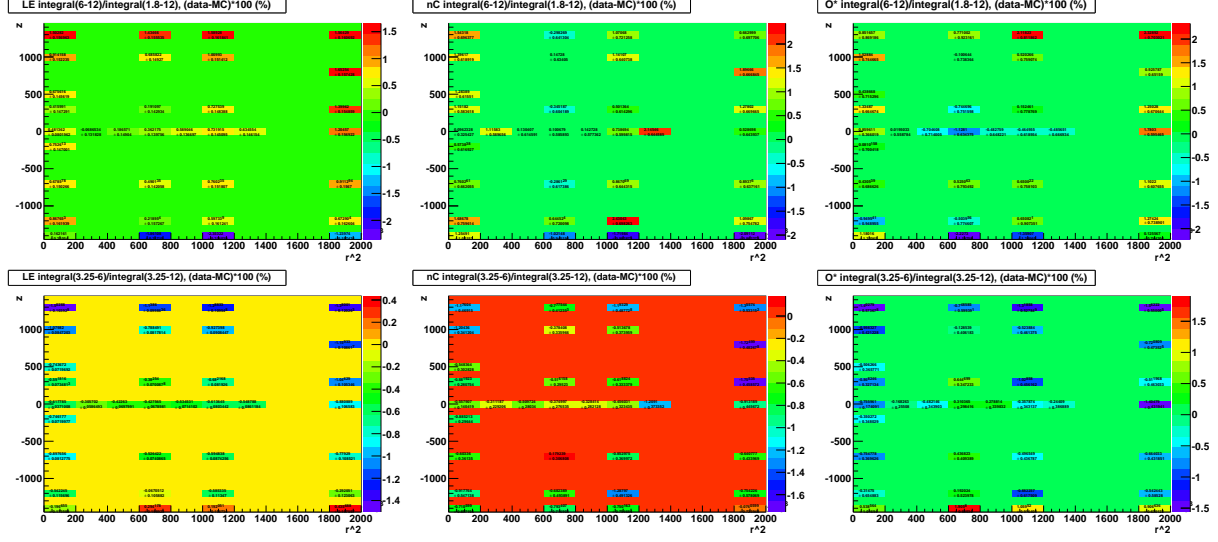


FIG. 24: Difference between tail shape ratios for MCS, plotted as data-MC in units of percent. The top row shows the ratio (3.25-6 MeV)/(3.25-12 MeV) and the bottom row shows the ratio (6-12 MeV)/(1.8-12 MeV). Three prompt integration windows: 0.7-3.5 MeV, the nC peak, and the O\* peak are given in the left, center, and right columns, respectively.

TABLE XIV: Difference between tail shape ratios, averages for Fig. 24. The top two rows show the weighted averages of all entries. The second two rows show the weighted averages excluding volumes at  $z = 0$  and  $r = (300, 500, 900, 1300)$  to give a more uniform distribution of samples. The fifth through eighth rows show the same, but using unweighted averages (i.e. assuming all volume elements have the weight=1). All differences are sub-percent.

	Low Energy prompts	nC peak	O* peak
(6-12 MeV)/(1.8-12 MeV)	$0.621 \pm 0.026$	$0.640 \pm 0.109$	$0.449 \pm 0.121$
(3.25-6 MeV)/(3.25-12 MeV)	$-0.642 \pm 0.014$	$-0.652 \pm 0.059$	$-0.416 \pm 0.068$
(6-12 MeV)/(1.8-12 MeV)	$0.666 \pm 0.027$	$0.611 \pm 0.117$	$0.585 \pm 0.130$
(3.25-6 MeV)/(3.25-12 MeV)	$-0.685 \pm 0.016$	$-0.687 \pm 0.065$	$-0.475 \pm 0.075$
(6-12)/(1.8-12)	$0.545 \pm 0.171$	$0.633 \pm 0.171$	$0.346 \pm 0.171$
(3.25-6)/(3.25-12)	$-0.628 \pm 0.171$	$-0.767 \pm 0.171$	$-0.337 \pm 0.171$
(6-12)/(1.8-12)	$0.573 \pm 0.183$	$0.600 \pm 0.183$	$0.447 \pm 0.183$
(3.25-6)/(3.25-12)	$-0.652 \pm 0.183$	$-0.791 \pm 0.183$	$-0.362 \pm 0.183$



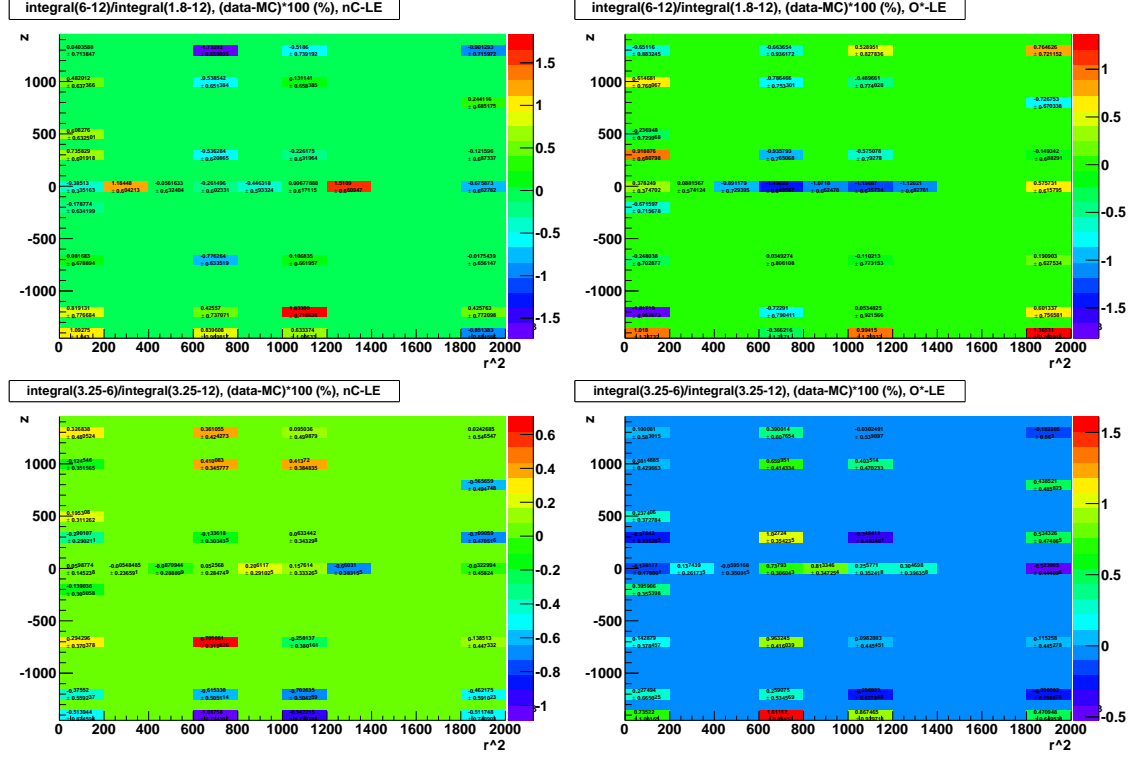


FIG. 25: The difference between prompt peaks projections for the differences between data and MC. For each row, the low-energy ratio plot is subtracted from the plots in Fig. 24.

TABLE XV: Difference of differences, averages for Fig. 25. The top two rows show the weighted averages of all entries. The second two rows show the weighted averages excluding volumes at  $z = 0$  and  $r = (300, 500, 900, 1300)$  to give a more uniform distribution of samples. The fifth through eighth rows show the same, but using unweighted averages (i.e. assuming all volume elements have the weight=1). All differences are sub-percent.

	nC-LE	O*-LE
$(6-12 \text{ MeV})/(1.8-12 \text{ MeV})$	$0.012 \pm 0.112$	$-0.185 \pm 0.124$
$(3.25-6 \text{ MeV})/(3.25-12 \text{ MeV})$	$-0.013 \pm 0.061$	$0.221 \pm 0.070$
$(6-12 \text{ MeV})/(1.8-12 \text{ MeV})$	$-0.062 \pm 0.120$	$-0.105 \pm 0.133$
$(3.25-6 \text{ MeV})/(3.25-12 \text{ MeV})$	$-0.001 \pm 0.067$	$0.210 \pm 0.077$
$(6-12)/(1.8-12)$	$0.088 \pm 0.171$	$-0.200 \pm 0.171$
$(3.25-6)/(3.25-12)$	$-0.139 \pm 0.171$	$0.291 \pm 0.171$
$(6-12)/(1.8-12)$	$0.026 \pm 0.183$	$-0.127 \pm 0.183$
$(3.25-6)/(3.25-12)$	$-0.139 \pm 0.183$	$0.290 \pm 0.183$

A careful reader may note that in the tables above, the differences of the averages is not equal to the average of the differences. One should not expect this equality to hold unless the data points have the same weight [23]. The volumes studied above are weighted according to the statistics of the MCS runs contained within them.

Overall, two main conclusions can be drawn from this data-MC comparison using the MCS. First, “tail shapes” (3.25-6 MeV/3.25-12 MeV) and “total neutron detection efficiency” (6-12 MeV/1.8-12 MeV) **differ by <0.8% between Monte-Carlo and data** (Tbl. XIV). Any delayed-energy efficiency studies based

only on MC should add this uncertainty to their overall uncertainty calculations. Second, the nGd tail shape does not strongly depend on neutron energy. The neutrons associated with the O\* prompt peak have lower kinetic energy than the neutrons associated with either the low-energy prompts or the nC prompt peak. However, **the differences in the tail shape ratios between O\* and nC or LE neutrons is typically <0.5%.**

### C. Summary

The total nGd detection efficiency is determined using IBD tail shape comparisons to be  $92.7\% \pm 0.9\%$ . This conclusion is supported by comparison of MCS PuC tail shapes in data and Monte Carlo for a wide range of neutron energies.

## VI. COMBINED EFFICIENCY

A separate calculation of the combined effects of the full-volume nGd capture fraction and the nGd detection efficiency can be measured by looking at the full-volume  $\epsilon_{Gd-combined}$  for the MCS data. This can also provide a good cross check to the systematics estimated for each component individually. This study was with two independent analyses, one described in the section above, and an additional study done in tandem with the MCS full-volume Gd capture fraction study described in section IV C. For details about event selection, background selection, etc., refer to this previous section.

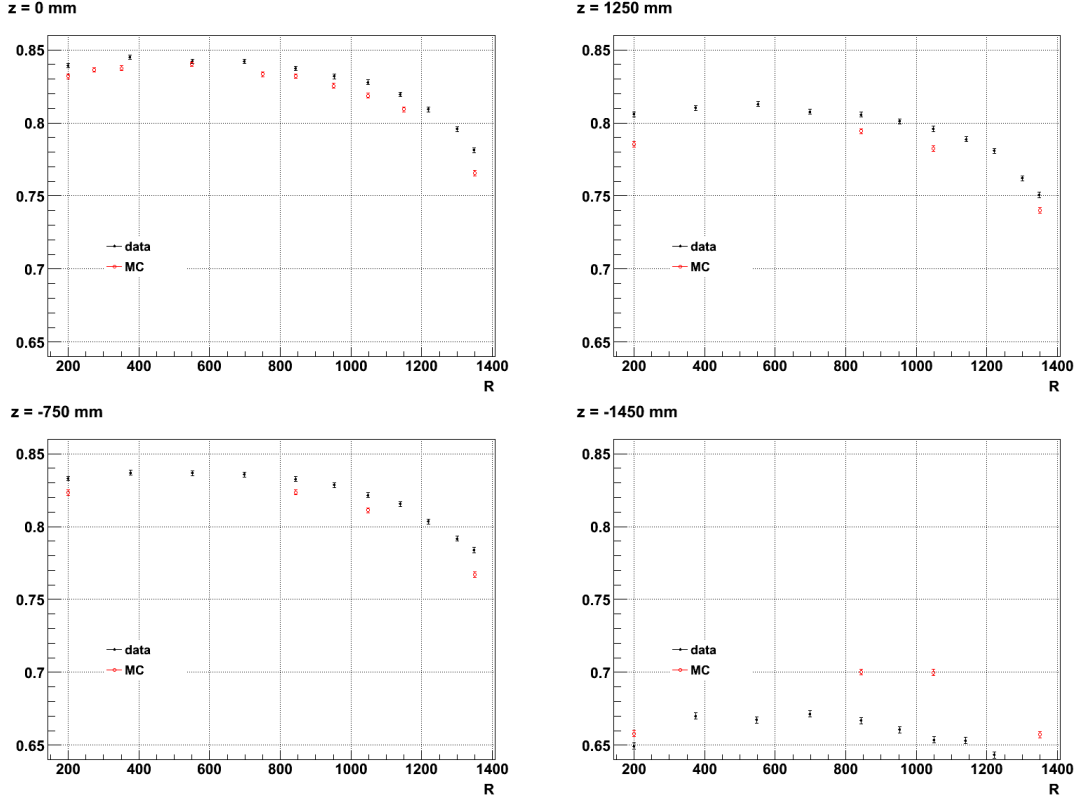


FIG. 26:  $\epsilon_{Gd-combined}$  R-dependence for data/MC

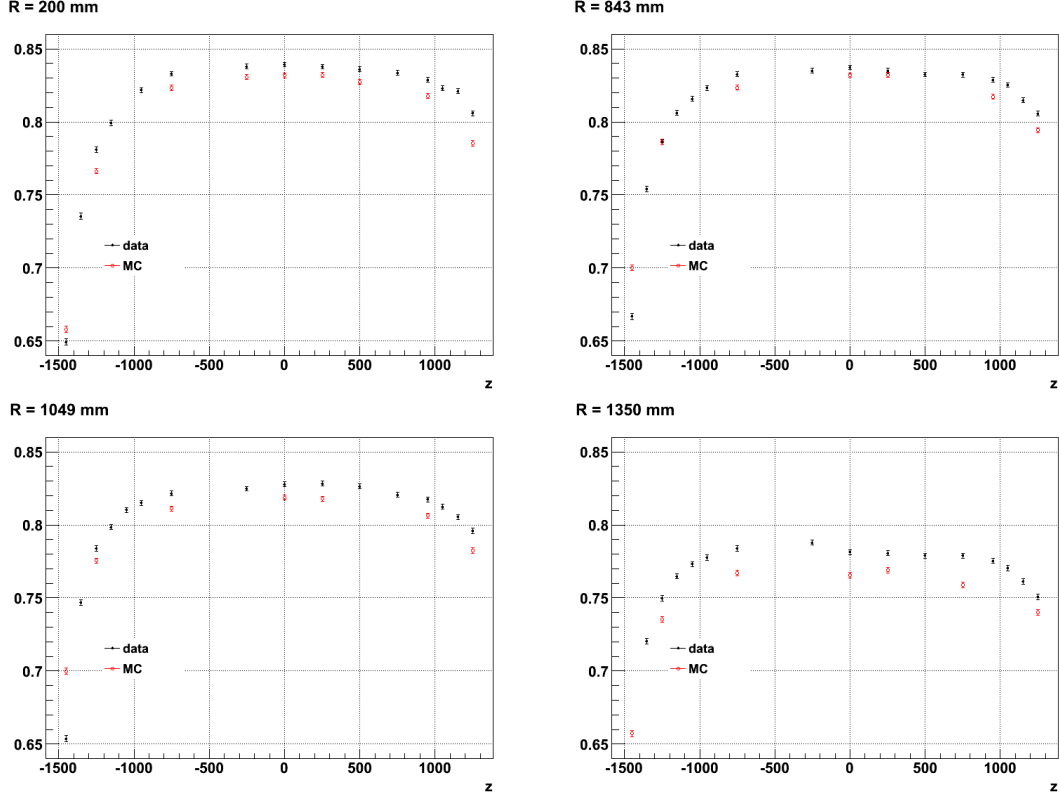


FIG. 27:  $\epsilon_{Gd-combined}$  Z-dependence for data/MC

Fig. 26, 27 show the R-, Z-dependence for  $\epsilon_{Gd-combined}$  for selected MCS data and MC. Obviously data/MC discrepancy is larger than that for  $\epsilon_{Gd-H}$ , which seems, at first sight, to agree with the IBD tail shape difference as shown in the next section for Gd Capture Detection Efficiency.

A fit for the  $\epsilon_{Gd-combined}$  was also performed using the same model given in Equations 7 and 6. As can be seen from Fig. 28, the  $\chi^2/ndf$  is not as good as that for  $\epsilon_{Gd-H}$ . Nevertheless, we can still use it to evaluate the data/MC difference. By varying the Z-dependence form and intergral window, the largest data/MC difference is found to be 1.3%. If we compare this 1.3% with the combination of the individual contributions from the nGd capture fraction and nGd detection efficiency, which is  $\sqrt{0.8^2 + 1.1^2}\% = 1.4\%$ , they are in good agreement.

We also looked at the data at phi angles other than 240 degree to see if there is any phi-dependence. No indications were observed. The variations for  $\epsilon_{Gd-H}$  and  $\epsilon_{Gd-combined}$  at different angles are within 0.3% and 0.5% respectively.

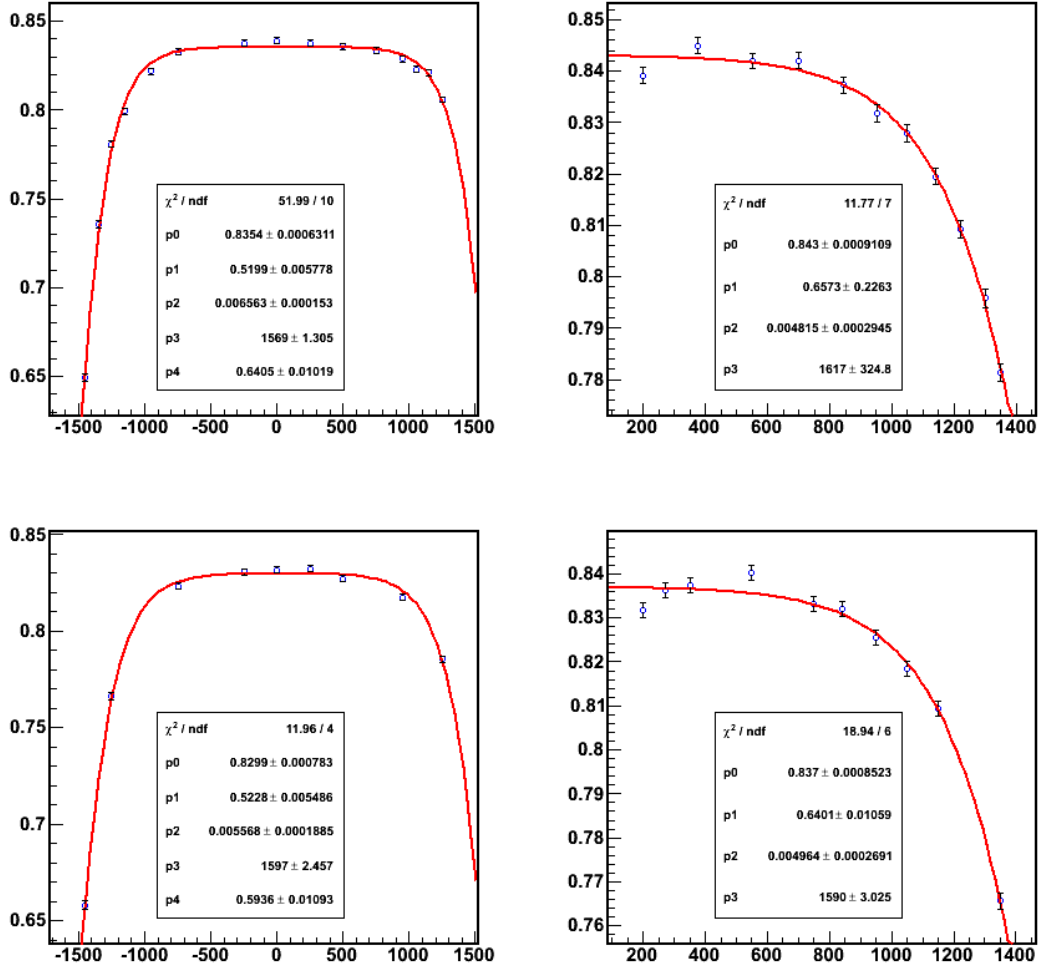


FIG. 28: Fit for  $\epsilon_{Gd-combined}$ . Upper(bottom) two plots for data(MC), left(right) two plots for Z-(R-) dependence.

TABLE XVI: Full-volume  $\epsilon_{Gd-combined}$  results. "Fixed" means the full-volume integral window is a fixed window  $[-1550, 1550]$  for Z and  $[0, 1550]$  for R; "Float" means the full-volume integral window depends on the fitting results, i.e.  $[-p_3, p_3]$  for Z and  $[0, p_3]$  for R. Asymmetric(Symmetric) denotes whether up-down Z-dependence asymmetry is allowed or not.

	Data	MC	Diff.
Fixed, Asymmetric	80.81%	79.91%	0.8%
Float, Asymmetric	80.55%	79.28%	1.3%
Fixed, Symmetric	80.18%	79.64%	0.5%
Float, Symmetric	79.76%	79.36%	0.4%

## VII. SPILL-IN EFFECTS

The first rate-only PRL quotes the spill-in enhancement as  $5\% \pm 1.5\%$ . The central value is from MC prediction, and the absolute uncertainty is from the difference of two MC models of neutron thermal scattering. [16]. One is free gas model when neutron got scattered on every atom, the other includes the molecular effect due to hydrogen bond in water when neutron scattered on hydrogen in scintillator. We choose the later model as the default one for MC sample production since it agrees data better in terms of capture time, especially for the neutron thermalization peak below  $10 \mu s$ .

In this technote, we'd like to shrink the uncertainty further to 1%. Several studies are included:

- MC spill-in prediction with variation of neutron scattering models
- neutron source calibration at ACUC(z=0)
- comparison of reconstructed vertex distribution: data vs MC
- comparison of capture time distribution: data vs MC

There is also a proposal to combine spill-out and spill-in effect in MC calculation to shrink the uncertainty further(docdb-10289), but the correlatoin between spill-in/out has not been investaged throughly. So we'll not discuss this topic here.

### A. MC prediction with modeling on neutron scattering

Currently the default model on neutron scattering adopts the thermal neutron scattering law on hydrogen of water below 4eV as suggested for water in Geant4, which has considered the hydrogen bond in water and the consequent energy transfer to neutron, or energy gain from neutron. While in the free gas model, no energy transfer will be considered. Besides hydrogen of water, Geant4 has inherited several other neutron thermal scattering data from ENDF for some common used moderators such as water, polyethylene, liquid ch4(lch4), graphite, etc. Most of those data are from theoretical calculation based on the density of state in the molecule and validated by some differential cross section measurements, however, no calculation or experimental data on scattering law(i.e. double differential cross section) is available for our DYB material such as LAB, acrylic, MO. Nevertheless, compared with free gas model, the model with hydrogen of water in scintillator significantly improve the agreement of capture time between data and MC. This give us the confidence on the neutron thermal scattering models. As a complementary study, several models of hydrogen scattering in some moderators are also tried in the simulation. Since hydrogen is the main scatterer, only free gas model are used for carbon and oxygen. Models in scintillator and acrylic vessels are changed separately. In total, 5 models are used:

- free gas
- H of water
- H of polyethylene
- H of PMMA(Poly(methyl methacrylate), i.e. acrylic)
- H of lch4(liquid ch4)

The acrylic model is evaluated by ourselves based on a density of state from private communication with a chemist, which is not published and hence has no too much quality guarantee(docdb-10064, docdb-10192).

As shown in Tab. XVII XVIII XIX XX XXI, with such variation in neutron scattering models, all the IBD spill-in are within 1% of the default MC prediction(4.9%) except for the case that both scintillator and acrylic are in free gas model(7.1%). Needless to say, free gas model in scintillator can't give better capture time spectrum than other neutron thermal scattering model. And we can also rule out this case with the neutron source at ACUC(z=0) axis, see section VII B.

TABLE XVII: H of water model in scintillator and models in acrylic.

scint model	acrylic model	IBD spill-in(%)
Water	Freegas	4.9
	PMMA	4.4
	Poly	4.3
	Water	4.3
	lch4	4.2

TABLE XVIII: H of polyethylene model in scintillator and models in acrylic.

scint model	acrylic model	IBD spill-in(%)
Poly	Freegas	4.9
	PMMA	4.5
	Poly	4.1
	Water	4.2
	lch4	4.15

TABLE XIX: H of PMMA model in scintillator and models in acrylic.

scint model	acrylic model in	IBD spill-in(%)
PMMA	Freegas	5.4
	PMMA	4.5
	Poly	4.3
	Water	4.3
	lch4	4.54

TABLE XX: H of liquid ch4 model in scintillator and models in acrylic.

scint model	acrylic model in	IBD spill-in(%)
lch4	Freegas	4.3
	PMMA	3.87
	Poly	3.60
	Water	3.71
	lch4	3.8

TABLE XXI: Free gas model in scintillator and models in acrylic.

scint model	acrylic model	IBD spill-in(%)
Freegas	Freegas	7.1
	PMMA	5.5
	Poly	5.1
	Water	4.9
	lch4	4.95

### B. $n\text{Gd}/n\text{H}$ : neutron source at ACUC( $z=0$ )

The idea to benchmark the spill-in effect via the ACUC neutron is very straight forward since those neutrons are created outside of target volume. Obviously, a Gd captured ACUC neutron must be a spill-in neutron. We can still define some observable in data, which should be directly relevant to spill-in effect, and the uncertainty for spill-in can be estimated via the data/MC comparison. Eventually we can quote the spill-in uncertainty for IBD neutron based on the uncertainty of ACUC neutron.

Several long AmC runs are taken and analyzed(docdb-8618). To quantify the spill-in effect for ACUC neutron, a  $n\text{Gd}/n\text{H}$  ratio can be defined with delayed signal region (6,12)MeV to tag the  $n\text{Gd}$  capture, and the another delayed signal region (1.9,3)MeV to tag the  $n\text{H}$  capture. The selection of the neutron capture sample is pretty IBD-like, the following cuts are applied in order: flasher cut,  $600\mu\text{s}$  WP muon veto and 1ms AD muon veto(otherwise specified in later different acc. background subtraction), only 2 events within a  $200\mu\text{s}$  time window, no other prompt-like events before or after the prompt-delayed pair, the delayed events fall into the energy range (1.9,3) MeV, or (6,12)MeV. After such selection, the samples are still contaminated by two kinds of backgrounds. One is the accidental background due to the Ge source and natural radioactivity, and the other one is the IBD events. Actually, the spill-in events from ACUC is in the same order with IBD events. The IBD background can be subtracted by a nearby physics run.

Fig. 29 shows the AD1 and AD2 result from long AmC run, and Fig. 30 shows the AD1/AD2 combined result, which show one the  $n\text{Gd}/n\text{H}$  ratio on different prompt recoil energy. In principle, the neutron scattering model that gives more IBD spill-in will also produce a larger  $n\text{Gd}/n\text{H}$  ratio. Fig. 31 shows the MC prediction with free gas model in both scintillator and acrylic. One can see that this modeling can be vetoed since the  $n\text{Gd}/n\text{H}$  from MC is larger than data at each prompt energy bin. This also rules out the most exception in IBD MC(7.1%, by free gas model in both scintillator and acrylic).

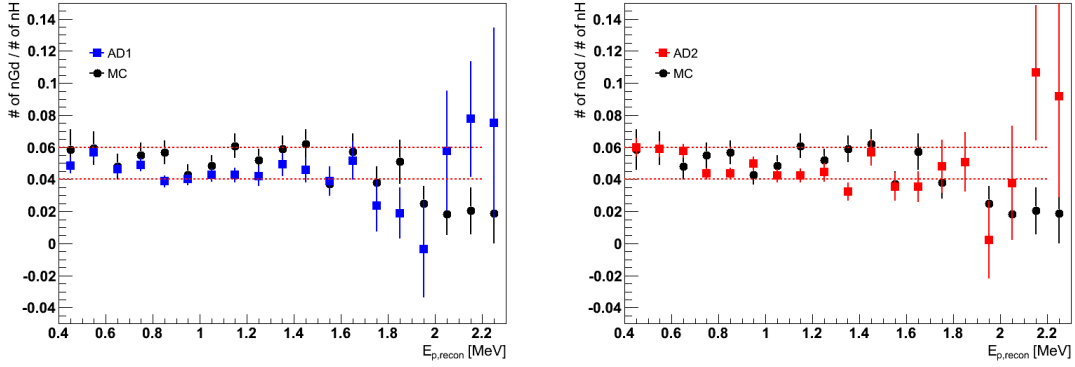


FIG. 29: Gd/H ratio in data, as well as MC.

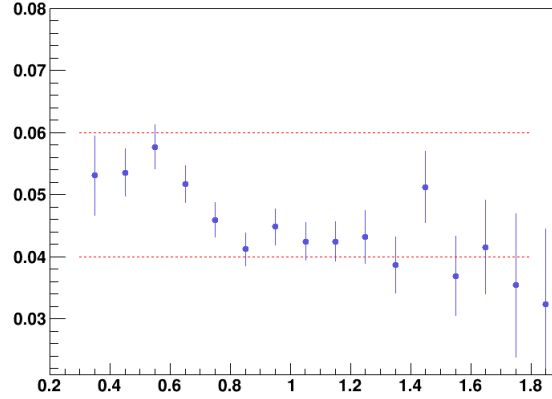


FIG. 30:  $n\text{Gd}/n\text{H}$  vs prompt energy for ACUC neutron(AD1 and AD2 combined)

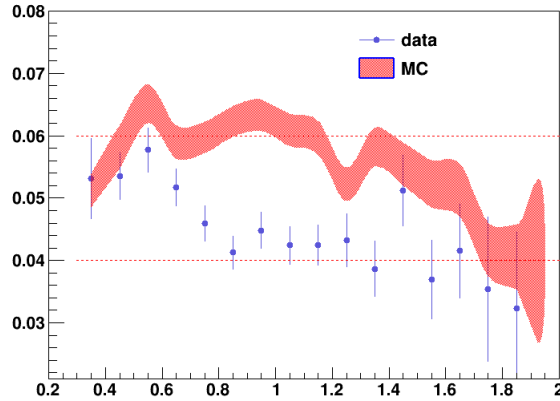


FIG. 31:  $n\text{Gd}/n\text{H}$  vs prompt energy, MC are also overlaid, with both free gas model in sintillator and in acrylic

### C. Reconstructed IBD Vertex: Data vs MC

If we have a good understanding of our detector response, MC simulation shall give us a good agreement on reconstructed vertex between data and MC. That is to say, the distribution will be different with the existence of any excess or deficit in spill-in component.

The reconstructed  $R^2$  distribution of IBD prompt from M14A is given in Figure 32 as well as the distribution from P14A data. To conservatively estimate the difference in spill-in effect between MC and data, one could assume that any difference in  $R_{rec}$  distributions between data and Monte Carlo is due to underestimation or overestimation of spill-in. Since spill-in events are mainly from the radial boundary of the acrylic vessel as in Fig. 37, the radius distribution will be compared with events from large reconstructed radius, say  $R^2 > 1.5\text{m}^2$ . Only AdSimple reconstruction is compared in this study as AdScaled doesn't provide a good agreement between data and MC.

In Fig. 32, the top two plots shows that data have more events at large radius ( $R^2 > 1.5\text{m}^2$ ) than MC prediction (1.5% more with accidental cut  $dr < 1\text{m}$ , and 1.2% more with accidental cut prompt energy larger than  $3.5\text{MeV}$ ).

However, from some calibration data, one can observe the non-perfect alignment between data and MC. For this reason, MCS data and MC will be compared with the true position. In Fig. 33, left plot shows the difference between true and reconstructed position for MCS deployments in various positions for data and MC. The wide variation in data at common  $R$  comes from variations in  $\phi$ , possibly resulting from gain differences between differing PMTs. In the right plot, data/MC discrepancy is evaluated along the true radius. Therefore, 1cm offset is assigned for AdSimple and 2.4cm for AdScaled. The IBD vertex comparisons after vertex correction are shown in the bottom two plots in Fig. 32. To conservatively estimate the discrepancy, both the negative and positive bins are included with their absolute value, and the difference between data and MC above  $1.5\text{m}^2$  is around 1.0% of total IBD sample.

### D. IBD coincidence time distribution and peak-to-tail(P/T) ratio: data vs MC

As can be seen in Fig. 34, the long tail component shows up in capture time distribution when the vertex get closer to the detector boundary. Such boundary effect is mainly due to the different neutron capture probability in two scintillator volumes, and consequently the different neutron mean free path. Therefore, the capture time variation near the boundary is strongly impacted by the neutron scattering models, so does the spill-in enhancement. It'll be helpful to see to what extent the IBD capture time in MC agrees with data. Any discrepancy might indicate a different spill-in fraction in data.



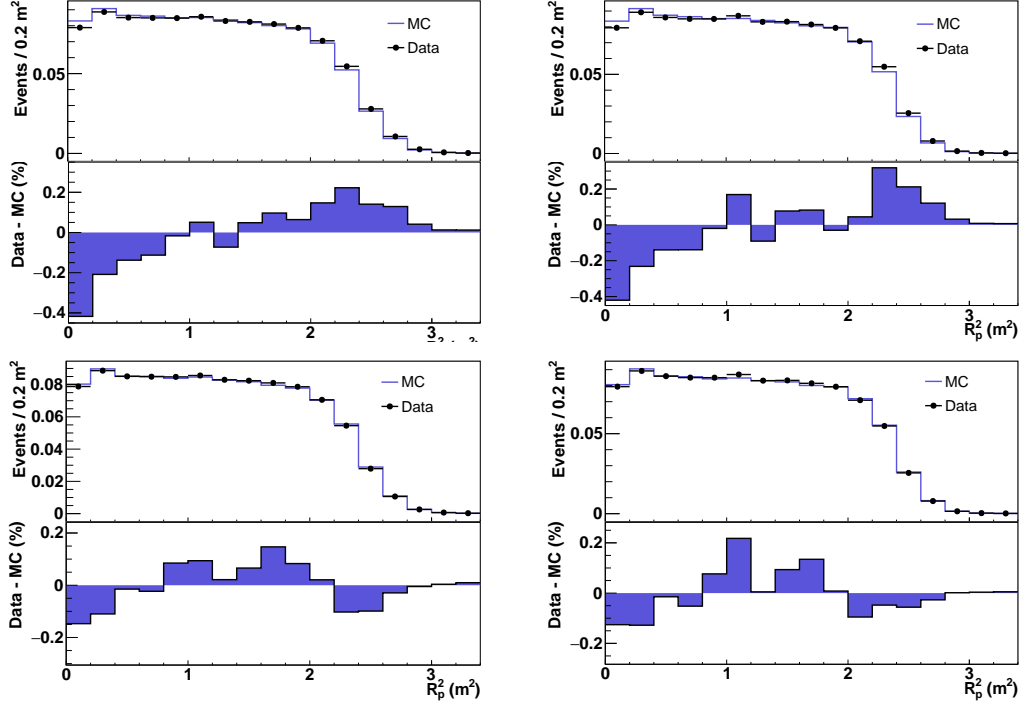


FIG. 32: Reconstructed  $R_p^2$  for IBD prompt: data vs MC. The top plots have no correction for reconstruction and data shows deviations to MC at about 30% of total spill-in events, that is to say, 1.5% of total IBD sample. Two accidental background cut is applied to data: one is prompt-deadly distance below 1m(left plot), the other is with prompt energy greater than 3.5MeV(right plot). While the bottom plots correct the vertex reconstruction biases using MCS data-MC comparisons. After such correction, the difference between data and MC is within 20% of the total spill-in events in the selected MC sample.(19% for accidental cut  $ep > 3.5$  MeV, 18% for  $dr < 1000$  mm.)

To quantify the deviation of capture time distribution, a peak-to-tail ratio is defined as demonstrated in Fig. 34, where a  $200\mu s$  coincidence time window is divided into a peak region and a tail region. A smaller peak-to-tail ratio indicates more spill-in fraction. Given the factor that if the neutron scattering model is biased, diffusion of the neutron from different vertex won't be equally biased, therefore, we won't simply compare the peak-to-tail ratio with the whole data sample from data and MC. A better way to extract the deficit of data to MC is to compare the peak-to-tail, i.e. the shape of the capture time, bin by bin.

As we see in Fig. 35, both spill-in fraction and peak-to-tail ratio in each reconstructed radius bin can be evaluated with the default MC IBD sample. The spill-in fraction and peak-to-tail ratio both have a monotonic relation with  $R_p^2$ . This ensures us to relate peak-to-tail ratio with spill-in fraction directly and parametrized with a function, see Fig. 36.

Fig. 37 shows the estimated spill-in component for each  $R_p^2$  bin in data. For each  $R_p^2$  bin in data, the P/T ratio is translated into a spill-in percentage based on the MC P/T lookup curve. Finally, data indicates 10% lower spill-in than MC, or roughly 0.5% of the total set of IBD candidates.

The systematic variation is also investigated with variation of accidental cuts for data, peak and tail definition, prompt or delayed vertex to be used in binning, or even w/ or w/o vertex correction on vertex reconstruction. All the results shown in Tab. XXII indicate spill-in deficit within 10% of MC prediction, or 0.5% of total IBD sample, with only two exceptions that indicates 1% deficit spill-in in data.

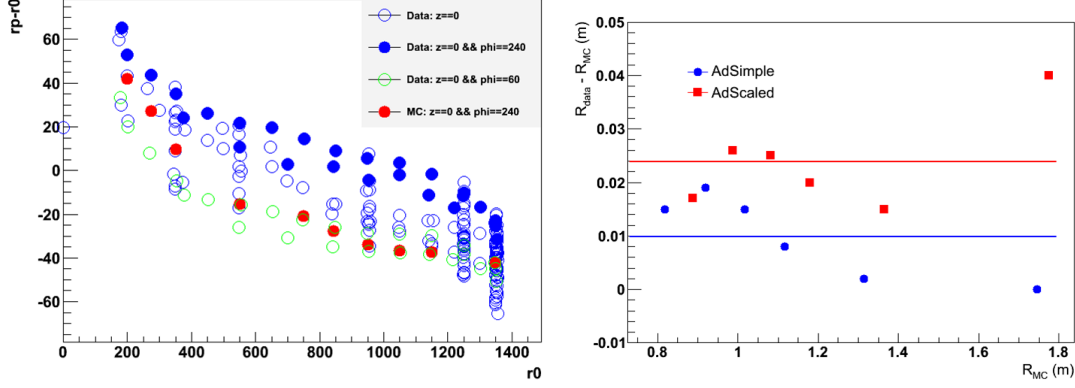


FIG. 33: Left: difference between true and reconstructed position for MCS deployments in various positions for data and MC. The wide variation in offset arises from the  $\phi$ -dependence of  $R_{rec}$ .

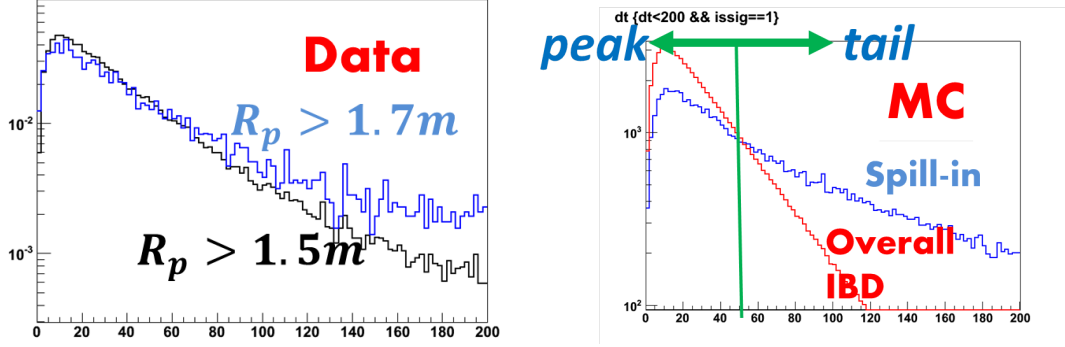


FIG. 34: Left: IBD timing spectrum in real data when different reconstructed vertex cuts are applied, showing the excess of spill-in events at large coincidence time. Right: an illustration of the peak-to-tail ratio definition.

### E. Summary

MC prediction on IBD spill-in agrees each other within 1% uncertainty by choosing different existing thermal neutron scattering laws from ENDF or acrylic law calculated by ourselves. The only exception can be vetoed by the neutron calibration in gamma catcher.

A comparison on IBD vertex is performed for data and MC with additional vertex correction indicated from MCS calibration, data agrees MC within 1% at large radius which indicates spill-in uncertainty is within 1%.

Meanwhile, IBD coincidence time spectrum is also quantified and compared between data and MC since the capture time deviation may indicate a different model of neutron scattering and therefore a different spill-in enhancement. With some systematic variations, the deviation of data from MC is believed to be within 0.5% with only two exceptions of 1%.

Therefore, we suggest to assign 1% uncertainty for spill-in enhancement, and keep 4.9% as central value.

## VIII. OTHER EFFICIENCIES

Other efficiencies contribute to the total absolute IBD detection efficiency. These uncertainties are generally much more well known than those absolute efficiencies described above. These efficiencies will not be

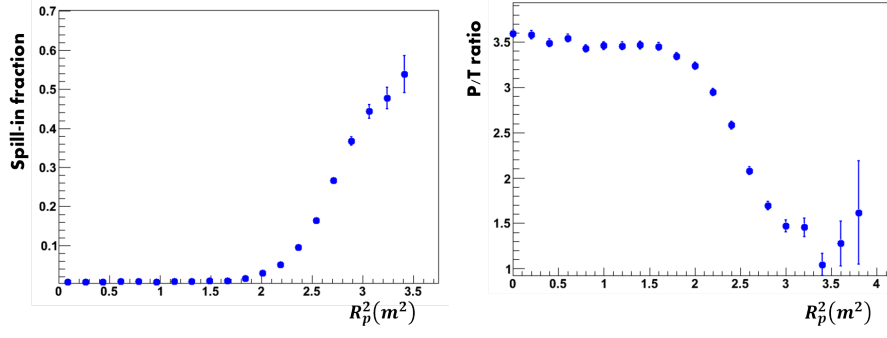


FIG. 35: peak-to-tail ratio and spill-in fraction in each bin versus  $R_p^2$

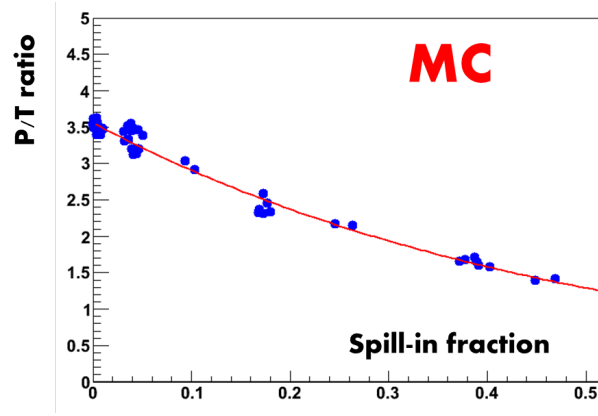


FIG. 36: The P/T ratio to spill-in fraction lookup curve calculated with MC sample.

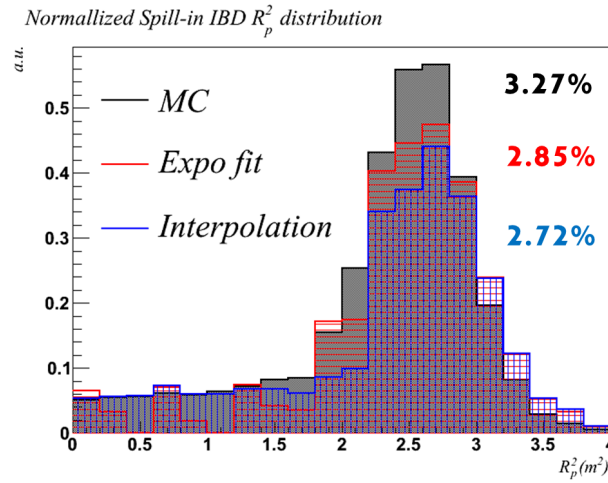


FIG. 37: Spill-in IBD's  $R_p^2$  distribution from MC and data. The red histogram is from exponential modeling based on the relation in Fig. 35, and the blue one is from interpolation method.

TABLE XXII: data and MC comparison with variations on some systematics

peak( $\mu$ s)	tail( $\mu$ s)			radius vertex correction(m)	prompt or delayed	accidental cut	data/MC
0	30	30	200	0.000000	prompt	dr<1m	0.907556
0	30	30	200	0.000000	prompt	ep>3.5MeV	0.994613
0	30	30	200	0.000000	delayed	dr<1m	1.071780
0	30	30	200	0.000000	delayed	ep>3.5MeV	1.214696
0	30	30	200	0.010000	prompt	dr<1m	0.905381
0	30	30	200	0.010000	prompt	ep>3.5MeV	0.998168
0	30	30	200	0.010000	delayed	dr<1m	1.075575
0	30	30	200	0.010000	delayed	ep>3.5MeV	1.218882
0	40	40	200	0.000000	prompt	dr<1m	0.924926
0	40	40	200	0.000000	prompt	ep>3.5MeV	0.904884
0	40	40	200	0.000000	delayed	dr<1m	1.023200
0	40	40	200	0.000000	delayed	ep>3.5MeV	0.929187
0	40	40	200	0.010000	prompt	dr<1m	0.923531
0	40	40	200	0.010000	prompt	ep>3.5MeV	0.907885
0	40	40	200	0.010000	delayed	dr<1m	1.032514
0	40	40	200	0.010000	delayed	ep>3.5MeV	0.940802
0	50	50	200	0.000000	prompt	dr<1m	0.909624
0	50	50	200	0.000000	prompt	ep>3.5MeV	0.903617
0	50	50	200	0.000000	delayed	dr<1m	0.938057
0	50	50	200	0.000000	delayed	ep>3.5MeV	0.966912
0	50	50	200	0.010000	prompt	dr<1m	0.912097
0	50	50	200	0.010000	prompt	ep>3.5MeV	0.904433
0	50	50	200	0.010000	delayed	dr<1m	0.944358
0	50	50	200	0.010000	delayed	ep>3.5MeV	0.974934
0	60	60	200	0.000000	prompt	dr<1m	0.903325
0	60	60	200	0.000000	prompt	ep>3.5MeV	0.936789
0	60	60	200	0.000000	delayed	dr<1m	0.923616
0	60	60	200	0.000000	delayed	ep>3.5MeV	0.900284
0	60	60	200	0.010000	prompt	dr<1m	0.904510
0	60	60	200	0.010000	prompt	ep>3.5MeV	0.934986
0	60	60	200	0.010000	delayed	dr<1m	0.928167
0	60	60	200	0.010000	delayed	ep>3.5MeV	0.904256

re-calculated here, and thus will only be very briefly mentioned.

### 1. Flasher Cut Efficiency

Spontaneous light emission from the Daya Bay PMT bases can mimic particle interactions of various energies. Flasher triggers can be easily rejected using charge topology cuts, whose characteristics and performance are described in detail in [1]. The signal efficiency of these cuts is estimated to be 99.98%.

## 2. Muon Veto Cut Efficiency

Cuts are also applied to reject coincident triggers correlated in time with muons traversing the water pools or ADs. The characteristics and performance of these cuts are also described in [1]. Total signal efficiencies for these cuts are roughly 82.0%, 85.8%, and 98.1% at EH1, EH2, and EH3, respectively.

## 3. Multiplicity Cut Efficiency

Some trigger coincidences containing more than two triggers are also rejected to avoid possible ambiguities in candidate prompt and delayed energy spectra. These multiplicity cuts are described in [1], and have an efficiency of 97.4% for all ADs, within 0.1%.

## 4. Capture Time Cut Efficiency

To be selected as signal the time coincidence of candidate triggers must be within a  $(1\mu\text{s}, 200\mu\text{s})$  range. As described in [1], and calculated with M13B MC, 98.7% of signal events will meet this criterion.

## 5. Prompt Energy Cut Efficiency

While the prompt energy cut is significantly below the 1MeV annihilation gamma energy, a small proportion of events (0.19%) deposit most of their energy in the non-scintillating inner acrylic vessel and fall below the 0.7 MeV cut threshold. This cut remains unchanged from that described in [1].

# IX. SUMMARY

Calculated absolute efficiencies and their related uncertainties are listed in Table XXIII. The absolute efficiency common to all detectors is 80.6%. Including multiplicity and muon veto efficiencies, which vary between detectors, total absolute efficiencies range from 64.4% in AD2 to 77.0% in AD6. The total fractional systematic uncertainty from detector efficiencies,  $\delta\epsilon/\epsilon$ , is 2.1%, and is contributed to mainly by uncertainties in the Gd capture ratio, nGd detection efficiency, and spill-in effects. This 2.1% estimate can be used as an input to the Daya Bay rate+shape oscillation fitter to determine the best-fit value and uncertainty bands of the absolute reactor flux normalization measurement.

Input	$\epsilon$	$\delta\epsilon$	$\delta\epsilon/\epsilon$
Target protons	-	-	0.47%
Flasher cut	99.98%	0.01%	0.01%
Muon veto cut	-	-	0.02%
Multiplicity cut	-	-	0.02%
Capture time cut	98.70%	0.12%	0.12%
Prompt energy cut	99.81%	0.10%	0.10%
Gd capture ratio	84.2%	0.8%	0.95%
nGd detection efficiency	92.7%	0.9%	0.97%
Spill-in correction	104.9%	-	1.50%
Combined	80.6%	-	2.08%

TABLE XXIII: Summary of absolute efficiencies and absolute systematic uncertainties. Note that uncertainties are given in both absolute and relative units. Combined uncertainty is given only in relative units.

- 
- [1] Daya Bay CPC paper, arXiv:[hep-ex]1210.6327
  - [2] Daya Bay PRL paper, arXiv:[hep-ex]1203.1669
  - [3] Doc-db 7525.
  - [4] Doc-db 7524.
  - [5] Doc-db 7273.
  - [6] Doc-db 9271.
  - [7] Doc-db 8467.
  - [8] Doc-db 8019.
  - [9] Doc-db 6700.
  - [10] Doc-db 9624.
  - [11] Doc-db 9222.
  - [12] Doc-db 4211.
  - [13] Doc-db 9574.
  - [14] Doc-db 9398.
  - [15] Doc-db 9453.
  - [16] Doc-db 7686.
  - [17] Doc-db 8112.
  - [18] Doc-db 8065.
  - [19] Doc-db 8466.
  - [20] Doc-db 8464.
  - [21] Doc-db 8618.
  - [22] The two histograms `AD1_FinalFullEvis` and `AD1_FinalFullEvisDelayed` are produced by `/people/Wisconsin/TreeAnalysis/printIBD.cxx`.
  - [23] A small program to demonstrate the differences in the means is not necessarily the mean of the differences is at [http://dayabay.ihep.ac.cn/svn/dybsvn/groups/AbsEff\\_TechNote/scripts/demo\\_diff\\_mean.cxx](http://dayabay.ihep.ac.cn/svn/dybsvn/groups/AbsEff_TechNote/scripts/demo_diff_mean.cxx).